

1 **The CESM2 Single Forcing Large Ensemble and Comparison to CESM1:**  
2 **Implications for Experimental Design**

3 Isla R. Simpson<sup>a</sup>, Nan Rosenbloom<sup>a</sup>, Gokhan Danabasoglu<sup>a</sup>, Clara Deser<sup>a</sup>, Stephen G. Yeager<sup>a</sup>,  
4 Christina S. McCluskey<sup>a</sup>, Ryohei Yamaguchi<sup>b</sup>, Jean-Francois Lamarque<sup>a</sup>, Simone Tilmes<sup>c</sup>,  
5 Michael J. Mills<sup>c</sup>, Keith B. Rodgers<sup>d,e</sup>

6 <sup>a</sup> *Climate and Global Dynamics Laboratory, National Center for Atmospheric Research, Boulder,*  
7 *Colorado*

8 <sup>b</sup> *Japan Agency for Marine-Earth Science and Technology, Yokosuka, Japan*

9 <sup>c</sup> *Atmospheric Chemistry Observations and Modelling Laboratory, National Center for*  
10 *Atmospheric Research, Boulder, Colorado*

11 <sup>d</sup> *Center for Climate Physics, Insitute for Basic Science, Busan, South Korea*

12 <sup>e</sup> *Pusan National University, Busan, South Korea*

13 *Corresponding author: Isla Simpson, islas@ucar.edu*

14 ABSTRACT: Single Forcing Large Ensembles are a relatively new tool for quantifying the con-  
15 tributions of different anthropogenic and natural forcings to the historical and future projected  
16 evolution of the climate system. This study introduces a new single forcing large ensemble with  
17 the Community Earth system Model version 2 which can be used to separate the influences of  
18 greenhouse gases, anthropogenic aerosols, biomass burning aerosols, and all remaining forcings,  
19 on the evolution of the Earth System from 1850 to 2050. Here, the forced responses of global near  
20 surface temperature and associated drivers are examined in CESM2 and compared with those in  
21 a single forcing large ensemble with CESM2's predecessor, CESM1. The experimental design,  
22 the imposed forcing and the model physics all differ between the CESM1 and CESM2 ensembles.  
23 In CESM1 an "all-but-one" approach was used where everything except the forcing of interest is  
24 time evolving, while in CESM2 an "only" approach is used, where only the forcing of interest is  
25 time evolving. This experimental design choice is shown to matter considerably for anthropogenic  
26 aerosol-forced change in CESM2, due to state dependence of cryospheric albedo feedbacks and  
27 non-linearity in the Atlantic Meridional Overturning Circulation (AMOC) response to forcing.  
28 This impact of experimental design is, however, strongly dependent on the model physics and/or  
29 the imposed forcing as the same sensitivity to experimental design is not found in CESM1, which  
30 appears to be an inherently less non-linear model in both its AMOC behavior and cryospheric  
31 feedbacks.

## 32 **1. Introduction**

33 Historically, the Earth’s climate system has evolved under a mixture of natural and anthropogenic  
34 forcings and it will continue to do so moving forward. A common approach that is used to  
35 disentangle and understand the relative contributions of such forcings to the evolution of the  
36 climate system is to perform Earth System Model (ESM) experiments in which only some forcings  
37 are evolving in time while others are held fixed. These experiments, which we will refer to as single  
38 forcing experiments even though they may be used to isolate the influence of multiple forcings at  
39 once, are most informative when a relatively large number of ensemble members are available, such  
40 that the forced signal can be isolated from the internal variability (e.g., Deser et al. 2020a). Many  
41 modelling centers have performed single forcing experiments under the coordinated framework of  
42 the “Detection and Attribution Model Intercomparison Project” (DAMIP, Gillett et al. 2016) as  
43 part of the Coupled Model Intercomparison Project (CMIP) and their utility has been recognized  
44 by the World Climate Research Program through emphasis on single forcing large ensembles as  
45 part of the lighthouse activity on “Explaining and Predicting Earth System Change” (Smith et al.  
46 2022).

47 Single forcing experiments have been a core component of Intergovernmental Panel on Climate  
48 Change (IPCC) reports and have been used to conclude that human influence has unequivocally  
49 warmed the climate (IPCC 2021; Gillett et al. 2021). Beyond this, they have been used to  
50 investigate the wide ranging impacts of individual forcings on various aspects of the climate system.  
51 These include: the global patterns of surface temperature and precipitation anomalies induced by  
52 greenhouse gas versus aerosol forcing (Deser et al. 2020b; Shi et al. 2022); the influence of aerosol  
53 forcing on precipitation in the Sahel region (Dong et al. 2014; Giannini and Kaplan 2019; Hirasawa  
54 et al. 2020; Zhang et al. 2021) and other monsoon regions of the world (Li et al. 2018; Undorf  
55 et al. 2018; Monerie et al. 2022); the influence of ozone depleting substances and greenhouse  
56 gases on precipitation over Australia (Delworth and Zeng 2014); assessment of the aerosol-forced  
57 contribution to trends in the Pacific Ocean (Allen et al. 2014; Dittus et al. 2021) ; assessment of the  
58 counteracting influence of greenhouse gases and aerosols on Arctic sea ice (Mueller et al. 2018)  
59 and Arctic temperatures (England et al. 2021); the impacts of individual forcings on the North  
60 Atlantic Ocean circulation (Watanabe and Tatebe 2019; Dagan et al. 2020; Baek et al. 2022) and  
61 global sea level rise (Fasullo et al. 2020); the impacts of land cover change and irrigation on surface

62 temperature and precipitation (Singh et al. 2018); and, the impact of individual forcings on various  
63 other aspects of the hydrological cycle and extreme weather (Chiang et al. 2021; Pendergrass et al.  
64 2019; Bonfils et al. 2020; Seong et al. 2021; Touma et al. 2021). Single forcing experiments can  
65 also provide a useful testbed for exploring model sensitivity to differences in imposed forcings  
66 (e.g., Fyfe et al. 2021) or for inter-comparing the response to forcings among models (e.g., Menary  
67 et al. 2020; Dittus et al. 2021).

68 In the design of single forcing experiments choices must be made. Under the DAMIP protocol,  
69 the forcing of interest is evolving in time while all others are held fixed at pre-industrial values,  
70 referred to as the “only” method, hereafter. Another option is to evolve all forcings in time *except*  
71 the one of interest and determine that forcings influence by differencing this experiment from an  
72 all forcing simulation, referred to as the “all-but-one” method, hereafter; this was the choice made  
73 for the single forcing large ensemble with the CESM1 model. There is also a choice as to what  
74 year forcings are held fixed at; DAMIP fixes them at 1850, while the CESM1 single forcing large  
75 ensemble fixed them at 1920. Whether these various design choices will produce the same answer  
76 as to a forcing’s influence will depend on whether there are substantial non-linearities or state  
77 dependencies in the system, and prior results have been mixed as to whether this is the case. Meehl  
78 et al. (2004) found the global mean temperature response to forcings was approximately linearly  
79 additive while Feichter et al. (2004) and Ming and Ramaswamy (2009) found that it was not. A  
80 more recent study by Deng et al. (2020) assessed additivity of the response of greenhouse gases  
81 and aerosols in time slice experiments with CESM1. They found that for global mean temperature,  
82 the influence of these forcings were approximately linearly additive but for other features, such as  
83 autumn Arctic sea ice cover and East Asian precipitation, non-linearities did exist.

84 Here, we present a new single forcing large ensemble with the Community Earth System Model  
85 version 2 (CESM2). The aims of this study are two-fold: (1) to introduce this new dataset  
86 that researchers can use to further probe the impacts of individual forcings on the evolution of  
87 the Earth system according to this model and (2) to understand differences in the global mean  
88 temperature and radiative responses between this single forcing large ensemble and its predecessor  
89 (the CESM1 single forcing large ensemble (Deser et al. 2020b)). With regards to the second  
90 goal, we find substantial differences in the anthropogenic aerosol-forced global mean near surface  
91 air temperature evolution between the CESM1 and CESM2 ensembles. Three factors have the

92 potential to contribute to this: differences in imposed aerosol emissions; differences in model  
93 physics; and, differences in the experimental design. Here, we make use of additional targeted  
94 experiments to attempt to isolate the relative role of the experimental design and, while this will  
95 be shown to have an influence, its impact is found to be sensitive to model physics and/or imposed  
96 forcings. The models, experimental design and methods are described in section 2. In section 3,  
97 we compare the global mean surface air temperature (GMST) response between the CESM2 and  
98 CESM1 single forcing large ensembles and reveal a substantial difference in the aerosol-forced  
99 response. In section 4, we then explore the influence of experimental design on the aerosol-forced  
100 GMST change in the CESM2 single forcing large ensemble and follow this with a comparison to  
101 CESM1 in section 5. Discussion and conclusions are provided in section 6.

## 102 **2. Models, Experiments and Methods**

### 103 *a. CESM2 and its single forcing experiments*

#### 104 1) THE MODEL

105 CESM2 is the latest generation Earth System Model developed by the U.S. National Center  
106 for Atmospheric Research in collaboration with others (Danabasoglu et al. 2020). The default  
107 configuration of CESM2, which was used to contribute experiments to CMIP6 (Eyring et al.  
108 2016), simulates the global coupled Earth system at approximately 1° horizontal resolution. The  
109 atmospheric component is the Community Atmosphere Model version 6 (CAM6, Bogenschutz  
110 et al. 2018) with a model top at ~40 km and 32 layers in the vertical. It is coupled to the Parallel  
111 Ocean Program version 2 (POP2) ocean model (Smith et al. 2010; Danabasoglu et al. 2012),  
112 the Community Land Model version 5 (CLM5, Lawrence et al. 2019) and the Community Ice  
113 Code version 5 (CICE5, Hunke et al. 2015) and all the simulations in this study have fixed ice  
114 sheets. We refer readers to Danabasoglu et al. (2020) for more details and to the following studies  
115 for evaluation of various aspects of CESM2: Lawrence et al. (2019) for the representation of  
116 land surface processes; Simpson et al. (2020) for the large scale atmospheric circulation and its  
117 variability; Meehl et al. (2020) for the representation of monsoons; Capotondi et al. (2020) for  
118 the representation of Pacific sea surface temperature variability; and, DuVivier et al. (2020) for  
119 the representation of sea ice. In this description, we focus on the aspects of CESM2 that are of  
120 particular relevance to the single forcing large ensemble.

121 Within CESM2 with CAM6, atmospheric greenhouse gas concentrations are prescribed as  
122 monthly time evolving global concentrations. Aerosol forcing is introduced into the model via  
123 emissions of black carbon (BC), particulate organic matter (POM), sulfur dioxide (SO<sub>2</sub>), sulfate  
124 (SO<sub>4</sub>) and secondary organic aerosol precursor gas (SOAG). In CAM6, the aerosol scheme is the  
125 four-mode Modal Aerosol Module (MAM4, Liu et al. 2016). This consists of a very simple sec-  
126 ondary organic aerosol scheme that does not include the oxidation of Volatile Organic Compounds  
127 and it is not interactively coupled to biogenic emissions (Tilmes et al. 2019). For carbonaceous  
128 aerosols, compared to its predecessor (MAM3, Liu et al. 2012), MAM4 contains an additional  
129 primary accumulation carbonaceous aerosol mode to allow for an explicit treatment of the micro-  
130 physical aging of primary carbonaceous aerosols. Hydrophobic BC and POM are emitted into  
131 this fourth primary aerosol mode, where they do not activate cloud condensation nuclei (CCN)  
132 and cannot be removed by wet deposition. Over time (of the order 2-3 days) they move into the  
133 hydrophilic accumulation mode, where they are available for cloud droplet activation as CCN and  
134 also participate in wet deposition. This explicit treatment of the aging of carbonaceous aerosol in  
135 MAM4 compared to MAM3, where ageing was instantaneous, has the overall effect of increasing  
136 the lifetime and subsequent burdens of BC and POM (Liu et al. 2016, and also discussed in the  
137 Appendix). The cloud microphysics scheme is version 2 of the Morrison-Gottelman scheme (MG2,  
138 Gottelman and Morrison 2015) which, unlike its predecessor in CESM1, now includes dependence  
139 of mixed-phase immersion freezing ice nucleation on aerosols, i.e., dust aerosol acts as ice nucle-  
140 ating particles on which super cooled liquid water or vapor can freeze. CAM6 does not have a  
141 prognostic representation of stratospheric or tropospheric ozone or volcanic aerosol and, therefore,  
142 these forcings are prescribed.

143 In CLM5, each grid cell is composed of multiple land units (vegetated, lake, urban, glacier and  
144 crop) and each land unit has a specified number of columns which are then divided up into multiple  
145 patches. These patches contain a plant or crop functional type (PFT or CFT) which is prescribed  
146 through a land use time series file. Land use and land cover change can, therefore, be introduced  
147 through specified evolution of the PFTs and CFTs within each land unit and/or varying the fractional  
148 area covered by the land unit components, which allows transitions between natural vegetation,  
149 crop and glacier land units (a new feature within CLM5). The land use time series specification also  
150 determines the soil texture, wood harvest, industrial Nitrogen fertilizer application amounts and the

151 area of the land surface equipped for irrigation. Irrigation is applied dynamically within the model  
152 to the irrigation-equipped area and is applied to achieve a target soil moisture level (Lombardozzi  
153 et al. 2020). When using biogeochemistry mode (as in the experiments here), leaf area index and  
154 canopy height are prognosed by the model. While CLM5 includes the simulation of fire internally,  
155 the current default is that this does not produce emissions that are seen by the atmosphere - biomass  
156 burning emissions to the atmosphere are prescribed from forcing datasets.

## 157 2) FORCINGS AND EXPERIMENTS

158 The CESM simulations used in the following analysis are summarized in Table 1. The baseline  
159 ensemble for the CESM2 single forcing large ensemble is the second set of 50 members of the  
160 CESM2 large ensemble (Rodgers et al. 2021). The CESM2 large ensemble, referred to as LENS2  
161 hereafter, is a 100-member ensemble of simulations run under CMIP6 historical forcings between  
162 1850 and 2014 and forcings of the Shared Socio-economic Pathway 3-7.0 (SSP3-7.0, Meinshausen  
163 et al. 2020) thereafter. A mixture of “macro” and “micro” initialization strategies were used  
164 to introduce ensemble spread where “macro” refers to initializing each model component from  
165 different years of the CESM2 pre-industrial control and “micro” refers to introducing ensemble  
166 spread through a round-off level perturbation applied to the initial atmospheric potential temperature  
167 field. The first and second set of 50 members of LENS2 are run with different biomass burning  
168 aerosol emissions over the period 1990 to 2020 (see Rodgers et al. (2021)). The first 50 members  
169 of LENS2 use the default CMIP6 biomass burning aerosol dataset, which contains higher levels of  
170 interannual variability during 1997-2014 compared to earlier and later periods due to the inclusion  
171 of satellite derived emissions. To avoid these artificial discontinuities in biomass burning aerosol  
172 variability, which has been shown to cause a rectified climate response in some regions (Fasullo  
173 et al. 2021; DeRepentigny et al. 2022), the second set of 50 members of LENS2 were run with a  
174 smoothed (11-year running mean) version of the biomass burning dataset which alters the emissions  
175 from 1990 to 2020. All of the CESM2 single forcing large ensemble experiments use the smoothed  
176 biomass burning emissions dataset, and are compared with the corresponding second 50-member  
177 set of LENS2 simulations (see supplemental Fig. 1 for a comparison of the smoothed and default  
178 CMIP6 biomass burning emissions).

179 TABLE 1. Summary of CESM experiments. The presence of a "1" or "2" in the experiment name indicates the  
 180 simulation was performed with CESM1 or CESM2, respectively.

Name	Period	Model	# Members	Description
LENS2	1850-2100	CESM2	50	All forcings evolving. CMIP6 Historical and SSP3-7.0 but with smoothed BMB
AAER2	1850-2050	CESM2	15	Only anthropogenic aerosols evolving. Other forcings fixed at 1850
GHG2	1850-2050	CESM2	15	Only greenhouse gases evolving. Other forcings fixed at 1850
BMB2	1850-2050	CESM2	15	Only biomass burning emissions evolving. Other forcings fixed at 1850
EE2	1850-2050	CESM2	15	Forcings other than AAER, GHG and BMB evolving. AAER, GHG and BMB fixed at 1850s
LENS1	1920-2100	CESM1	40	All forcings evolving. CMIP5 Historical and RCP8.5 forcings
XAAER1	1920-2080	CESM1	20	All forcings evolving except anthropogenic aerosols which are kept fixed at 1920s levels
XGHG1	1920-2080	CESM1	20	All forcings evolving except greenhouse gases which are kept fixed at 1920s levels
XBMB1	1920-2030	CESM1	15	All forcings evolving except biomass burning which is kept fixed at 1920s levels
XAAER2	1920-2050	CESM2	3	All forcings evolving except anthropogenic aerosols which are kept fixed at 1920s levels
AAER1	1850-2050	CESM1	3	Only anthropogenic aerosols evolving. Other forcings fixed at 1850

181 As summarized in the top portion of Table 1, the CESM2 single forcing large ensemble consists of  
 182 four sub-ensembles of 15 members each that run from 1850 to 2050 following the “only” approach  
 183 where *only* the forcing(s) of interest are evolving in time and others are held fixed at 1850s values:  
 184 the greenhouse gas ensemble (GHG2); the anthropogenic aerosol ensemble (AAER2); the biomass  
 185 burning aerosol ensemble (BMB2) and the “Everything Else” ensemble (EE2), where the number  
 186 2 in each acronym refers to CESM2. The ensemble members differ through a macro initialization,  
 187 i.e., they are initialized from different years of the pre-industrial control simulation (the same  
 188 years as members 1-10 and 91-95 of LENS2) to minimize any effects of ocean persistence on  
 189 ensemble spread from the beginning of the run. In GHG2, only greenhouse gas concentrations  
 190 are evolving in time and all other forcings are held fixed at their 1850s values. Fig. 1a shows the  
 191 time-evolution of two of the important greenhouse gases (CO<sub>2</sub> and CH<sub>4</sub>) and others can be seen in  
 192 supplemental Fig. 2. In AAER2, only “anthropogenic aerosol” emissions are evolving in time. By  
 193 “anthropogenic aerosols” here, we refer to industrial, agricultural, domestic and transport related  
 194 emissions and acknowledge that this is not *all* anthropogenic emissions because it does not include  
 195 anthropogenic influences on biomass burning (e.g., van Marle et al. 2017). The global emissions of  
 196 three of the main aerosols or aerosol pre-cursors (SO<sub>2</sub>, BC and SO<sub>4</sub>) in the AAER2 ensemble are  
 197 shown in Fig. 1b and others can be seen in supplemental Fig. 3. In BMB2 only biomass burning  
 198 emissions are evolving in time, with three of the main emissions sources shown in Fig. 1c and



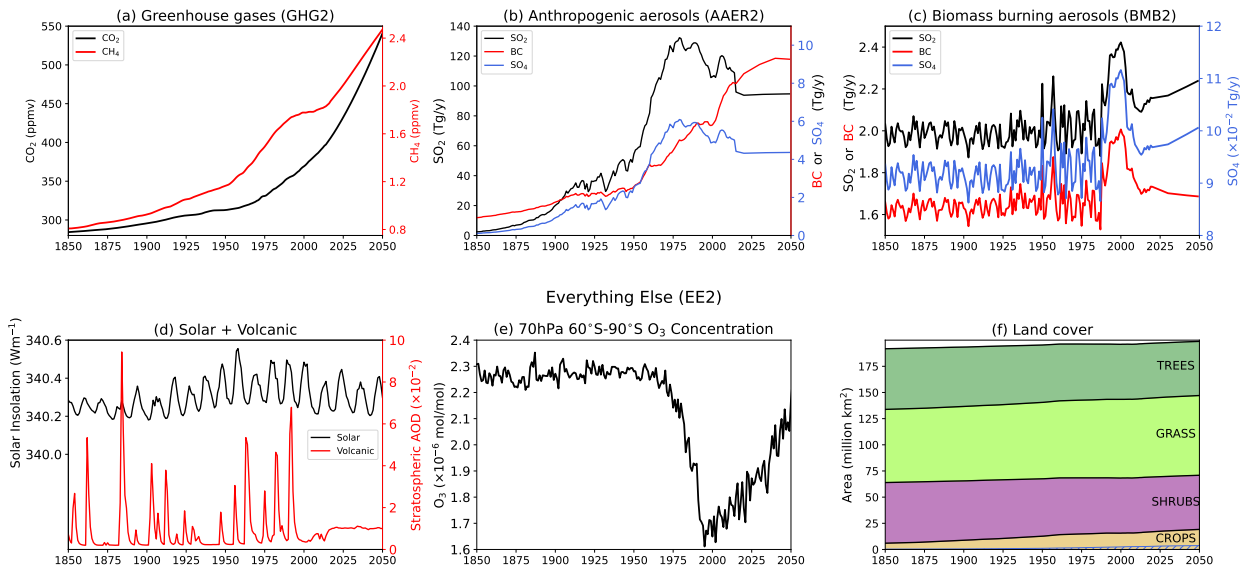
199 others shown in supplemental Fig. 1. The transitions in variance of biomass burning emissions  
200 between the historical portion, the smoothed 1990-2020 period, and then the subsequent SSP3-7.0  
201 projection period are quite apparent and this should be improved upon in any emissions datasets  
202 that are developed in the future. All other forcings, aside from those that are time evolving in  
203 GHG2, AAER2 and BMB2 are time evolving in the EE2 ensemble. Some of the main forcings that  
204 are evolving in this ensemble are the solar insolation (Fig. 1d black), the stratospheric volcanic  
205 aerosol (Fig. 1d red), stratospheric and tropospheric ozone (Fig. 1e for Southern Hemisphere (SH)  
206 stratospheric ozone) and land use and land cover change (Fig. 1f). The stratospheric volcanic  
207 aerosol and tropospheric and stratospheric ozone concentrations are derived from the average of a  
208 three-member ensemble of simulations with the Whole Atmosphere Community Climate Model  
209 version 6 (WACCM6, Gettelman et al. 2019), also run under historical and SSP3-7.0 forcings.  
210 This choice was made for all CESM2 experiments to limit forcing differences between CESM2  
211 and CESM2-WACCM and, given the similarity between CESM2 and CESM2-WACCM in the  
212 troposphere and lower stratosphere, the CESM2-WACCM ozone and volcanic aerosol fields will  
213 be more consistent with the model dynamics and atmospheric structure than the CMIP6 forcing  
214 datasets. Overall, each forcing is time evolving in one of these sub-ensembles, allowing the  
215 additivity of forcing contributions to be tested.

216 The CESM2 pre-industrial control simulation is also used to examine the behavior of the Atlantic  
217 Meridional Overturning Circulation (AMOC). This simulation is run for 2000 years under forcings  
218 that are representative of 1850s conditions, following the CMIP6 protocol and we make use of  
219 simulation years 400 to 2000.

## 227 *b. CESM1 and its single forcing experiments*

### 228 1) THE MODEL

229 CESM1 is the previous generation of CESM released in 2010 (Hurrell et al. 2013). It has been  
230 widely used, including through the CESM1 large ensemble (Kay et al. 2015) and the CESM1 single  
231 forcing large ensemble (Deser et al. 2020b). Between CESM1 and CESM2, major developments  
232 were undertaken in the atmosphere and land components, in particular. The atmospheric component  
233 of CESM1 is CAM5 and this contains the older aerosol scheme, MAM3, which, as discussed above,  
234 does not allow for the explicit treatment of the aging of primary carbonaceous aerosols although



220 FIG. 1. Annual means of selected forcings and their evolution in the single forcing ensembles. (a) Global CO<sub>2</sub> (left axis) and  
 221 CH<sub>4</sub> (right axis) concentrations as they evolve in the GHG2 ensemble. (b) Global emissions of SO<sub>2</sub> (left axis) and BC and SO<sub>4</sub>  
 222 (right axis) as they evolve in the AAER2 ensemble. (c) Global emissions of SO<sub>2</sub> and BC (left axis) and SO<sub>4</sub> (right axis) as they  
 223 evolve in the BMB2 ensemble. (d) - (f) show various forcings that evolve in the “Everything Else” ensemble: (d) Solar insolation  
 224 (left axis) and stratospheric Aerosol Optical Depth (AOD) from the WACCM6 simulations that produced the volcanic aerosol  
 225 forcing (right axis); (e) 70hPa ozone concentration averaged over 60°S to 90°S; and (f) surface area covered by various land cover  
 226 types (blue hatching shows the irrigated land surface area) and note that bare ground is not shown.

235 the representation of secondary organic aerosols is the same as in MAM4. The cloud microphysics  
 236 scheme is the first version of the Morrison-Gottelman scheme (MG1, Morrison and Gottelman  
 237 2008) which does not relate mixed-phase immersion freezing ice nucleation to aerosols. In CAM6,  
 238 many other atmospheric parameterizations underwent development compared to CAM5. For  
 239 example, CAM5 uses an older generation parameterization of shallow convection and boundary  
 240 layer turbulence compared to CAM6 and it has a simpler representation of orographic drag.

241 The land component of CESM1 is CLM4 (Lawrence et al. 2011). As with the atmosphere, the  
 242 CLM5 model component of CESM2 contains major developments compared to this older model  
 243 version. Major updates were performed on the representation of soil and plant hydrology, snow  
 244 density, river modeling, carbon and nitrogen cycling and crop modeling. These updates are, in  
 245 general, found to lead to improvements in the representation of many land surface processes in  
 246 the newer generation of the model (Lawrence et al. 2019) with impacts on the representation of  
 247 climate variability (e.g., Simpson et al. 2022). Of relevance for the prescription of time evolving  
 248 forcings, CLM4 does not allow for the time-evolution of the fractional area of each grid point  
 249 covered by different land cover types, e.g., it does not allow for transitions in the weighting of

250 natural vegetation versus crops within a grid cell, just time-evolution of the plant functional types  
251 within a given land cover type. It has a much simpler representation of crops and it does not have  
252 a representation of irrigation.

## 253 2) FORCINGS AND EXPERIMENTS

254 Forcings within CESM1 are prescribed in a similar manner to CESM2. Greenhouse gases  
255 are represented by prescribed global surface concentrations and aerosols are introduced through  
256 emission sources. Solar variability is introduced through variations in the total solar irradiance,  
257 time evolving volcanic aerosols and ozone concentrations are prescribed and land use and land cover  
258 change is introduced via time evolving plant functional types. CMIP5 era forcings are used in the  
259 CESM1 experiments. Historical forcings are used prior to 2005 and forcings of the Representative  
260 Concentration Pathway 8.5 (RCP8.5) are used thereafter (Meinshausen et al. 2011; Lamarque et al.  
261 2011). Much like for CESM2, the ozone forcing in the CESM1 experiments is prescribed based  
262 on WACCM simulations (in this case using WACCM4 and a two member ensemble with a 10-year  
263 running mean applied to each month of ozone forcing separately). In CESM1 the volcanic aerosol  
264 forcing does not come from WACCM, but rather CMIP5 forcing is used.

265 As summarized in the second portion of Table 1, the baseline ensemble for CESM1 is the CESM1  
266 large ensemble (Kay et al. 2015), referred to as LENS1 hereafter. This is a 40-member ensemble  
267 that runs from 1920 to 2100 in which all forcings are evolving, with each member differing  
268 through a round-off level perturbation introduced to the atmospheric potential temperature field  
269 at initialization (micro initialization). The CESM1 single forcing large ensemble (Deser et al.  
270 2020b) consists of 3 sub-ensembles of 15 or 20 members that use the “all-but-one” method where  
271 all forcings are time evolving except the forcing of interest, which is held fixed at the values for  
272 1920. Ensemble spread is also introduced through micro initialization and we refer to these sub-  
273 ensembles as XFORCING where X denotes that FORCING is held fixed. In the XGHG1 ensemble  
274 all forcings are evolving except greenhouse gases, in the XAAER1 simulation all forcings except  
275 anthropogenic aerosols are evolving (again, by anthropogenic aerosols here, we do not include  
276 anthropogenic influences on biomass burning) and, in the XBMB1 ensemble all forcings except  
277 biomass burning are evolving. The number 1 here denotes that these are CESM1 simulations. The  
278 time-evolution of the biomass burning emissions, greenhouse gas concentrations and anthropogenic

279 aerosol emissions in CESM1 can be compared with those in CESM2 in supplementary Figs. 1 to 3.  
280 Note that a fourth ensemble was originally included in which all forcings except land use and land  
281 cover change were evolving but this dataset has since been retracted due to an error. The XGHG1  
282 and XAAER1 ensembles extend from 1920 to 2080 and the XBMB1 ensemble extends from 1920  
283 to 2030. Given that the “all-but-one” approach is used, the influence of a given forcing must be  
284 determined by taking the difference between LENS1 and the XFORCING ensemble and because  
285 not all forcings are represented within an XFORCING ensemble, a complete test of additivity  
286 cannot be performed.

287 Years 400 to 2200 of the CESM1 pre-industrial control simulation are also used. This simulation  
288 was run under forcings that are representative of 1850s conditions, following the CMIP5 protocol.

### 289 *c. Experimental design sensitivity tests*

290 As will be shown, substantial differences in the inferred response to aerosol forcing are found  
291 between CESM1 and CESM2. To test the influence of the method used, i.e., “only” versus  
292 “all-but-one”, we perform 3-member ensembles of an “only” anthropogenic aerosol experiment  
293 with CESM1, referred to as AAER1 and an “all-but-one” anthropogenic aerosol experiment with  
294 CESM2, referred to as XAAER2, as summarized in the bottom portion of Table 1. In AAER1,  
295 CESM1 is run with time evolving anthropogenic aerosol forcing from 1850 to 2050 with all other  
296 forcings held fixed at 1850s values and members differ through micro initialization. In XAAER2,  
297 CESM2 is run from 1920 to 2050 with all forcings evolving except anthropogenic aerosols which  
298 are held fixed at those of 1920 and the members differ via macro initialization.

### 299 *d. Methods*

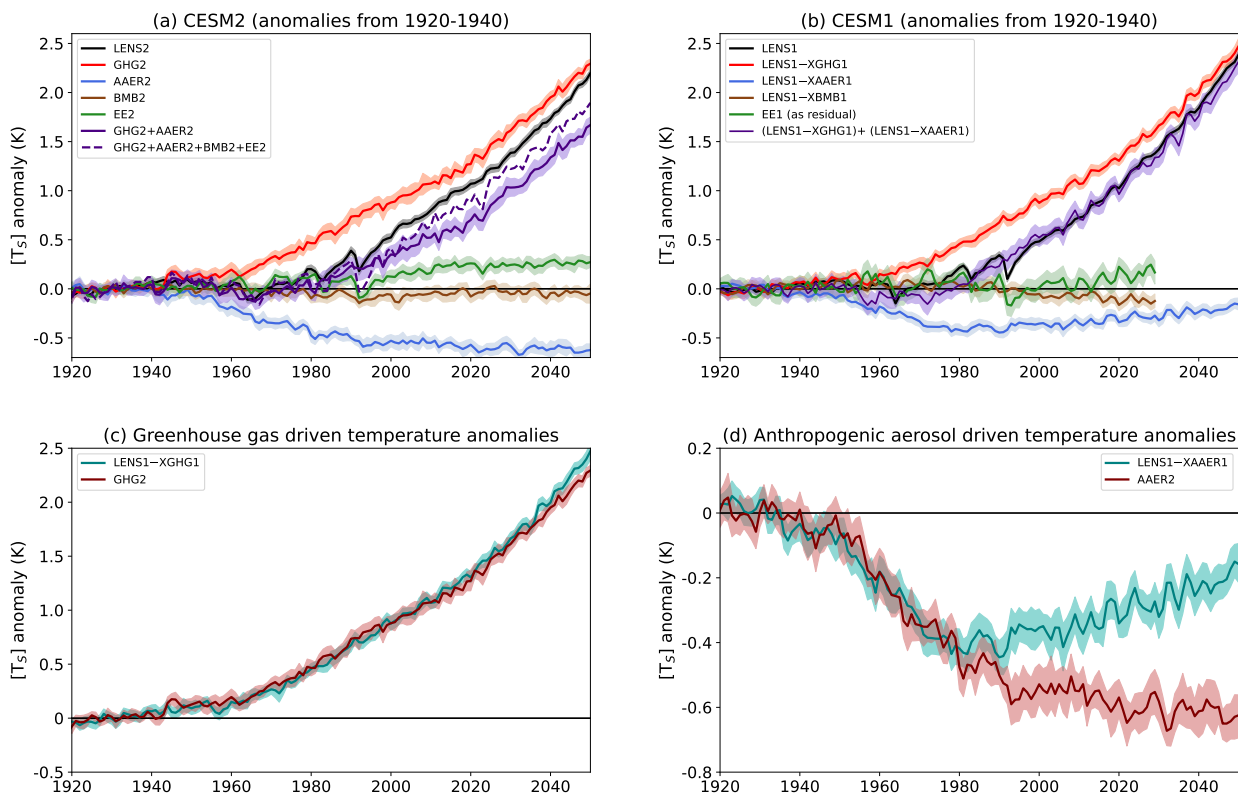
300 We focus on the period 1920 to 2050, which is common to the majority of CESM simulations  
301 (Table 1), and, unless otherwise stated, we consider ensemble mean anomalies from the 1920-1940  
302 average, which is at the beginning of the CESM1 single forcing large ensemble. For CESM1 the  
303 influence of a given forcing at a given time period is therefore given by the difference between  
304 LENS1–XFORCING at that time period and LENS1–XFORCING averaged over 1920 to 1940.  
305 For CESM2, the influence is simply given by the difference between that time period and the  
306 average of 1920 to 1940 for the single forcing ensemble.

307 To quantify uncertainty and statistical significance a bootstrapping approach is used whereby,  
308 within each ensemble, members are randomly sampled with replacement and a new ensemble mean  
309 calculated. This is repeated 1000 times and the uncertainty range on anomalies for that ensemble  
310 is given by the 2.5th to 97.5th percentile range of those bootstrapped ensemble means. For the  
311 3-member sensitivity tests, rather than performing bootstrapping on the 3-member ensembles,  
312 we either compare them to uncertainty ranges on the larger ensembles that are calculated by  
313 subsampling 3 members with replacement or we estimate uncertainty and significance levels  
314 by bootstrapping equivalent sample sizes from the respective pre-industrial control, under the  
315 assumption that the internal variability of the 1850s climate is representative of that throughout the  
316 simulation.

### 317 **3. Global mean surface air temperature evolution: CESM2 versus CESM1**

318 We begin by comparing the evolution of global mean near surface (2-m) air temperature ( $[T_s]$ ,  
319 and we will use  $[x]$  throughout to denote the global mean of variable  $x$ ) between the CESM2 single  
320 forcing large ensemble and CESM1 single forcing large ensemble in Fig. 2. Recall that the CESM1  
321 single forcing large ensemble does not have all forcing contributions represented, as the equivalent  
322 of the “Everything Else” ensemble was not performed. We, therefore, estimate the CESM1  
323 “Everything Else” contribution as the residual  $LENS1 - ((LENS1 - XGHG1) + (LENS1 - XAAER1)$   
324  $+ (LENS1 - XBMB1))$  for comparison with EE2. This can only be done out to 2030 when the  
325 XBMB1 simulation ends and assumes linearity, which may not be valid.

326 Figure 2a shows the time-evolution of  $[T_s]$  for LENS2 (black) and the contributions that are  
327 inferred to be due to the different forcing components. This can be compared with the equivalent  
328 for CESM1 in Fig. 2b. In both CESM1 and CESM2 greenhouse gases (red) act to increase  
329  $[T_s]$ , while anthropogenic aerosols (blue) act to decrease it. The role of biomass burning aerosols  
330 (brown) in  $[T_s]$  evolution is fairly minimal, while “Everything Else” (green) acts to cool the planet  
331 during the major volcanic eruptions of the 20th Century (e.g., El Chichon in the early 1960s and  
332 Pinatubo in the early 1990s) and to warm the planet relative to 1920-1940 throughout the first half  
333 of the 21st Century (most apparent in CESM2 where the EE contribution can be examined beyond  
334 2030). Exactly what is producing this warming warrants further investigation but it is potentially  
335 related to the lack of large volcanic eruptions in the projected future forcings (Fig. 1d, red).



326 FIG. 2. Time evolution of global mean surface air temperature anomalies relative to the 1920 to 1940 average for (a) CESM2  
 327 and (b) CESM1 and their respective single forcing large ensembles. For CESM1, the equivalent of “Everything Else” has been  
 328 estimated as a residual (green) of the difference between LENS1 and the sum of the greenhouse gas, anthropogenic aerosol and  
 329 biomass burning aerosol contributions. The solid purple line shows the sum of the greenhouse gas and anthropogenic aerosol  
 330 contributions and in panel (a) the dashed purple line shows the sum of all 4 components (GHG2 + AAER2 + BMB2 + EE2). (c)  
 331 Reproduces the greenhouse gas-forced anomalies for CESM1 and CESM2 for a more direct comparison while (d) is the same but  
 332 for the anthropogenic aerosol contribution. The shading uncertainty range is a 95% confidence interval on the ensemble mean  
 333 calculated by bootstrapping members with replacement.

344 In the CESM1 single forcing large ensemble, the capacity for exploring additivity is limited,  
 345 but we can see that the greenhouse gas contribution inferred from LENS1–XGHG1 and the  
 346 anthropogenic aerosol contribution inferred from LENS1–XAAER1 approximately add up to the  
 347 overall LENS1  $[T_s]$  anomalies (compare black and purple in Fig. 2b). This, however, is not true in  
 348 CESM2 (compare black and solid purple in Fig. 2a) where the sum of the  $[T_s]$  anomalies in GHG2  
 349 and AAER2 fall short of the LENS2  $[T_s]$  anomalies from the late 20th century onwards. Adding  
 350 in the contributions from BMB2 and EE2 brings the sum a little closer to LENS2 (dashed purple  
 351 in Fig. 2a) but a discrepancy still exists. It is clear from comparison of the relation between the  
 352 solid purple and black lines in Figs. 2a and b that the sum of the greenhouse gas and anthropogenic

353 aerosol contributions and how that relates to the all forcing signal differs considerably between  
354 CESM1 and CESM2.

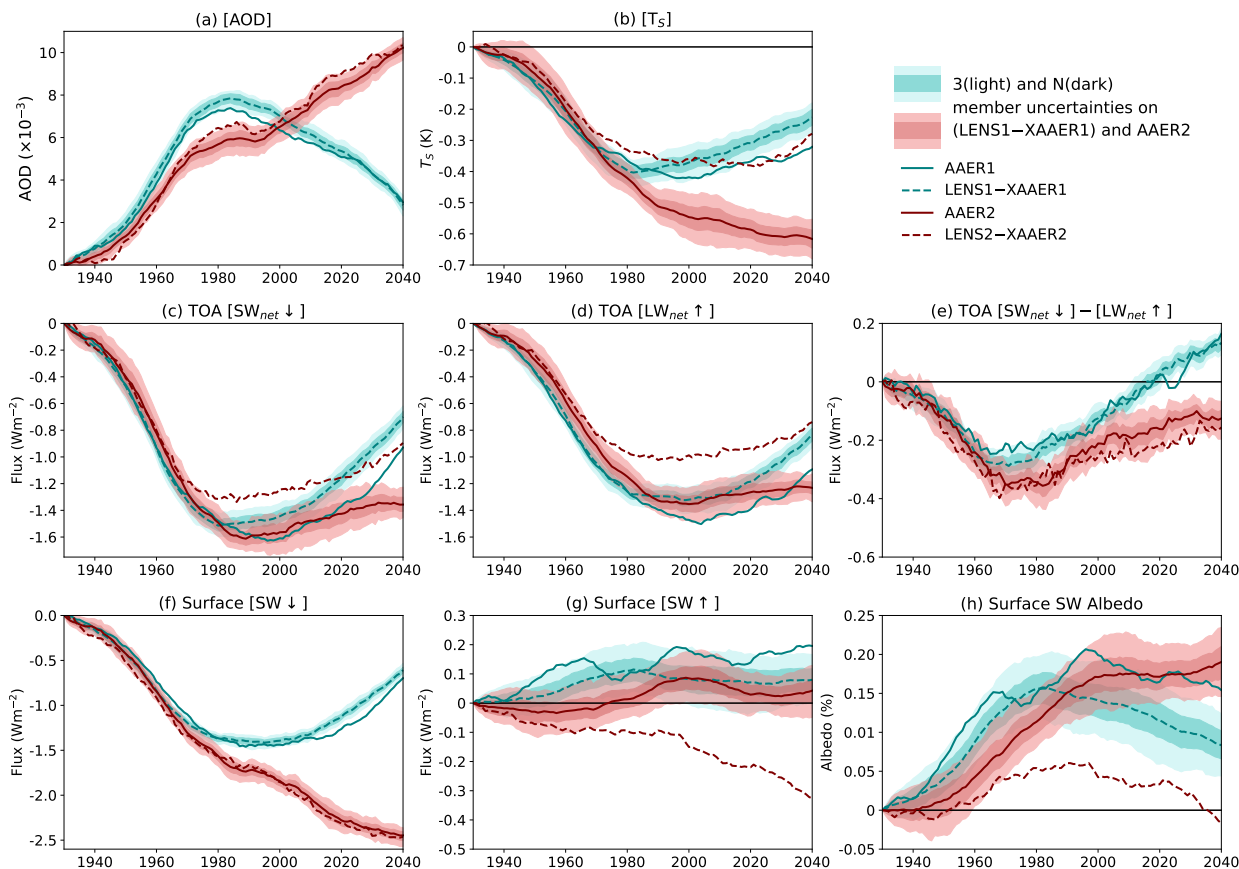
355 The prescribed GHG concentrations are rather similar between CESM1 and CESM2 over the  
356 period shown (supplemental Fig. 2) and a closer comparison of the GHG-forced signals between  
357 CESM1 and CESM2 (Fig. 2c) reveals that the GHG-forced  $[T_s]$  anomalies are also comparable  
358 between CESM1 and CESM2. Note that this is not true locally as GHG2 warms more than  
359 LENS1–XGHG1 in the low latitudes but warms much less in the Northern Hemisphere (NH)  
360 high latitudes - a feature that will be discussed further in section 5 . CESM1 and CESM2 differ  
361 considerably in the global mean  $[T_s]$  anomalies due to anthropogenic aerosol forcing (Fig. 2d).  
362 Anthropogenic aerosols continue to cool the planet out to 2050 in CESM2 while the anthropogenic  
363 aerosol induced cooling in CESM1 maximizes in the 1980s and then declines, such that by 2050, the  
364 global mean anthropogenic aerosol-forced  $[T_s]$  anomalies differ by about 0.4K between CESM1 and  
365 CESM2. This difference in anthropogenic aerosol-forced  $[T_s]$  change could be due to differences  
366 in the experimental design, differences in the aerosol emissions, differences in the model physics  
367 or some combination of these, as explored in the following sections.

#### 368 **4. The impact of the single forcing method on the aerosol-forced response**

##### 369 *a. Global mean temperature and radiative fluxes*

370 A major difference between the CESM1 and CESM2 single forcing large ensembles is the  
371 experimental design. In CESM1, an “all-but-one” approach was used while in CESM2 an “only”  
372 approach was used. To test the influence of this experimental design, we consider the additional  
373 three-member ensembles: XAAER2, where the anthropogenic aerosol simulation of CESM2 was  
374 performed in the same way as with CESM1; and, AAER1, where the anthropogenic aerosol  
375 simulation of CESM1 was performed in the same way as CESM2.

376 Time series of 21-year running mean anomalies (chosen as a reasonable balance between reducing  
377 noise, while retaining features of the time-evolution) of various global mean quantities are shown  
378 in Fig. 3 for each of the methods for both CESM1 and CESM2. First, it is worth noting the  
379 substantial differences in the global mean AOD between the CMIP5 and the CMIP6 forcings (Fig.  
380 3a). This is primarily due to the differences in emissions but there is also a contribution from the  
381 enhanced lifetime of black carbon in CESM2 (see the Appendix). [AOD] continues to rise out to



388 FIG. 3. Global mean centered 21-year running means of annual means of anomalies relative to 1920 to 1940 of various fields from  
 389 AAER1 (teal solid), LENS1-XAAER1 (teal dashed), AAER2 (maroon solid) and LENS2-XAAER2 (maroon dashed). Shaded  
 390 ranges are shown around the experiments with the large ensembles (LENS1-XAAER1 and AAER2) with the light component  
 391 showing the uncertainty on a 3-member mean of XAAER1 or AAER2 and the dark component showing the uncertainty for an  
 392  $N$ -member mean of XAAER1 or AAER2 where  $N$  is the number of members in the anthropogenic aerosol single forcing ensemble.  
 393 (a) Aerosol optical depth at 500nm, (b) near surface air temperature, (c) top of atmosphere (TOA) net downward shortwave flux, (d)  
 394 top of atmosphere net upward longwave flux, (e) top of atmosphere net downward radiative flux, (f) surface downward shortwave  
 395 flux, (g) surface upward shortwave flux, (h) albedo.

382 2050 in CESM2 but declines after about 1980 in CESM1 and the experimental design does not  
 383 substantially impact the [AOD] evolution (compare solid and dashed in Fig. 3a). A comparison  
 384 of the burdens of different aerosol species in Fig. A1 and supplemental Fig. 4 indicates, perhaps  
 385 unsurprisingly, that the difference in [AOD] trends between AAER1 and AAER2 is dominated by  
 386 the differing trends in anthropogenic aerosols as opposed to sea salt or dust which can respond as  
 387 the climate changes under anthropogenic aerosol forcing.

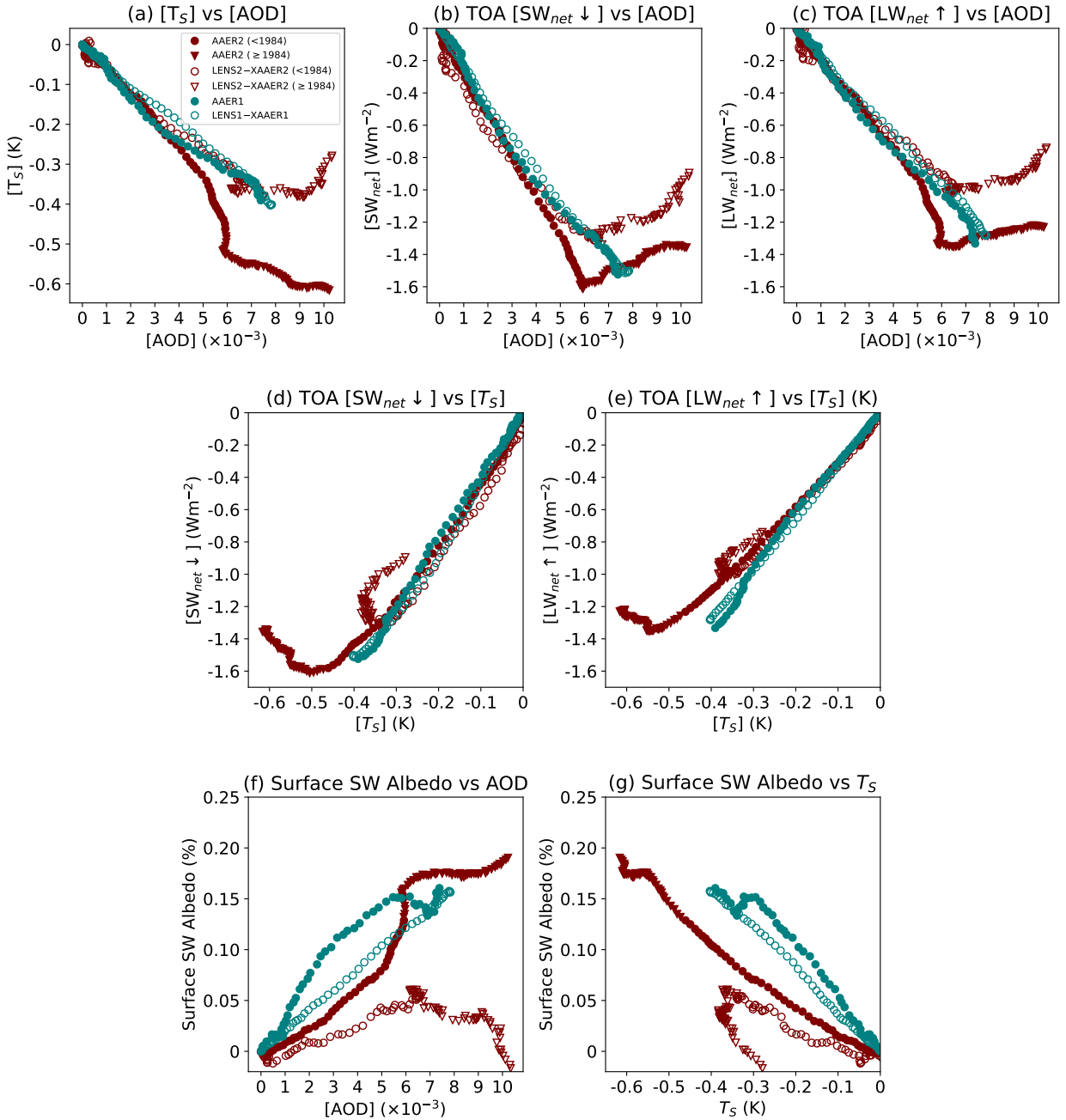
396 It is clear from the  $[T_s]$  time series in Fig. 3b that the experimental design has a substantial  
 397 impact on the inferred anthropogenic aerosol influence on  $[T_s]$  in CESM2. When the aerosol  
 398 forcing is imposed in isolation (solid maroon in Fig. 3b), much colder temperature anomalies are



399 reached than when the aerosol influence is inferred from LENS2–XAAER2 (dashed maroon in  
400 Fig. 3b), with the difference in the aerosol-forced cooling being  $\sim 0.3\text{K}$  by 2030-2050. Note that  
401 the difference between LENS2–XAAER2 and AAER2 is much greater than would be expected  
402 due to sampling uncertainty alone (compare dashed maroon with the light uncertainty shading on  
403 the solid maroon in Fig. 3b). The result is that when the anthropogenic aerosol influence is inferred  
404 from LENS2–XAAER2, the overall cooling is more comparable to the cooling found in CESM1  
405 (compare maroon dashed with teal in Fig. 3b). This indicates a strong sensitivity of the inferred  
406 aerosol cooling to the experimental design (“all-but-one” versus “only”) in CESM2. In CESM1,  
407 the AAER1 simulation (solid teal) is also significantly cooler than LENS1–XAAER1 (dashed teal)  
408 toward the end of the simulation, but the impact of the experimental design in CESM1 is relatively  
409 minor compared to that found in CESM2. We will revisit this difference between CESM1 and  
410 CESM2 in section 5 and for now focus on the dependence on the experimental design within  
411 CESM2.

412 In Fig. 4a it can be assessed how  $[T_s]$  varies as a function of  $[AOD]$ . Here, we only show the  
413 variations over the time period when  $[AOD]$  is increasing, which means for CESM1, we are showing  
414 out to the 21-year mean centered on 1984, while for CESM2 we are showing out to the end of the  
415 simulation. Fig. 4a shows that up to  $[AOD]$  anomalies of about  $8 \times 10^{-3}$  (the maximum in CESM1)  
416 the evolution of  $[T_s]$  as a function of  $[AOD]$  is rather similar in each of AAER1, LENS1–XAAER1  
417 and LENS2–XAAER2. In contrast, AAER2 cools a lot more at a given  $[AOD]$  for  $[AOD]$  greater  
418 than around  $4 \times 10^{-3}$ . In addition, the evolution of  $[T_s]$  as a function of  $[AOD]$  is non-linear,  
419 particularly in LENS2–XAAER2. In the 21st century, the cooling in LENS2–XAAER2 levels off  
420 and then turns around and the planet starts to warm even while the  $[AOD]$  continues to increase  
421 (Fig. 3a versus b and Fig. 4a).

422 To begin to understand the difference between AAER2 and LENS2–XAAER2, consider the  
423 top of atmosphere (TOA, although actually here the fluxes used are at the model top) radiative  
424 fluxes and their imbalance shown in Figs. 3c-e. Fig. 3e shows the difference between the net TOA  
425 downward shortwave radiation ( $[SW_{net} \downarrow]$ ) and the net TOA upward longwave radiation ( $[LW_{net} \uparrow]$ ),  
426 i.e., the TOA radiative imbalance. Throughout we refer to fields that are positive when downward  
427 with the down arrow ( $\downarrow$ ) and fields that are positive when upward with the up arrow ( $\uparrow$ ). The way  
428 in which the overall TOA radiative imbalance evolves is similar between the methods (compare  
429  
430  
431  
432  
433



422 FIG. 4. Global mean 21-year running means of annual means. Both CESM1 and CESM2 are only shown for the period over  
 423 which [AOD] is continuing to increase, which means the full record is shown for CESM2, but only up to the 21-year mean centered  
 424 on 1984 is shown for CESM1. The CESM2 points transition from circles to triangles after 1984. (a)-(c) show  $[T_s]$ , TOA net  
 425 downward shortwave and TOA net upward longwave, respectively, versus [AOD]. (d) and (e) show TOA net downward shortwave  
 426 and TOA net upward longwave versus  $[T_s]$  and (f) and (g) show surface shortwave albedo versus (f) [AOD] and (g)  $[T_s]$ .

434 solid and dashed in Fig. 3e). However, the evolution of the separate components  $[SW_{net} \downarrow]$  (Fig.  
 435 3c) and  $[LW_{net} \uparrow]$  (Fig. 3d) is not - they reveal that this same TOA radiative imbalance is achieved  
 436 for rather different reasons.

437 Until about 1980, aerosol forcing causes TOA [ $SW_{net} \downarrow$ ] to decline as aerosols and associated  
438 cloud changes reflect more shortwave radiation back to space and as surface albedo increases. In  
439 AAER2, after about 1970, there is a greater decline in TOA [ $SW_{net} \downarrow$ ] than in LENS2–XAAER2,  
440 but this difference is opposed by a greater decline in [ $LW_{net} \uparrow$ ], such that the overall TOA radiative  
441 imbalance ends up roughly the same in each case. The greater decline in [ $LW_{net} \uparrow$ ] in AAER2  
442 can be attributed to the greater decline in [ $T_s$ ]; a colder planet emits less longwave radiation to  
443 space. Indeed, Fig. 4e shows that [ $LW_{net} \uparrow$ ] depends on [ $T_s$ ] in a rather similar way in AAER2 and  
444 in LENS2–XAAER2 but AAER2 cools further and, in association with this, [ $LW_{net} \uparrow$ ] declines  
445 more. So, overall, while the TOA radiative imbalance evolves in a similar way in AAER2  
446 and in LENS2–XAAER2, it reflects different quasi-equilibria with differing balances between  
447 TOA [ $LW_{net} \uparrow$ ] and TOA [ $SW_{net} \downarrow$ ]<sup>1</sup>. Overall, we infer that the reason AAER2 cools more than  
448 LENS2–XAAER2 lies in the behavior of the shortwave radiation. TOA [ $SW_{net} \downarrow$ ] declines more  
449 in AAER2 and this is balanced by a greater cooling and greater reduction in TOA [ $LW_{net} \uparrow$ ].

450 The greater decline in TOA [ $SW_{net} \downarrow$ ] in AAER2 compared to LENS2–XAAER2 must arise  
451 from a difference in the shortwave radiation being reflected back to space, either from within  
452 the atmosphere or from the surface. Fig. 3 demonstrates that it is the difference reflected back  
453 from the surface that is key to the TOA [ $SW_{net} \downarrow$ ] differences. If the key were differences in  
454 the extent to which shortwave radiation is reflected back to space from within the atmosphere,  
455 either by aerosols themselves or the associated cloud radiative effects, then we would expect to see  
456 differences in the surface downward shortwave radiation ([ $SW \downarrow$ ]), but Fig. 3f makes it clear that  
457 the anomalies in [ $SW \downarrow$ ] are very similar between AAER2 and LENS2–XAAER2. The decline in  
458 surface [ $SW \downarrow$ ] is independent of which method is used in both CESM1 and CESM2, although the  
459 response differs substantially between them in association with their differing aerosol forcings. In  
460 contrast, Fig. 3g demonstrates a clear difference in the surface upward shortwave ([ $SW \uparrow$ ]) between  
461 AAER2 and LENS2–XAAER2 in association with a difference in their surface shortwave albedo  
462 responses (Fig. 3h). In AAER2, the surface shortwave albedo increases much more than in  
463 LENS2–XAAER2. As a result, surface [ $SW \uparrow$ ] stays roughly constant in AAER2 (Fig. 3g), even

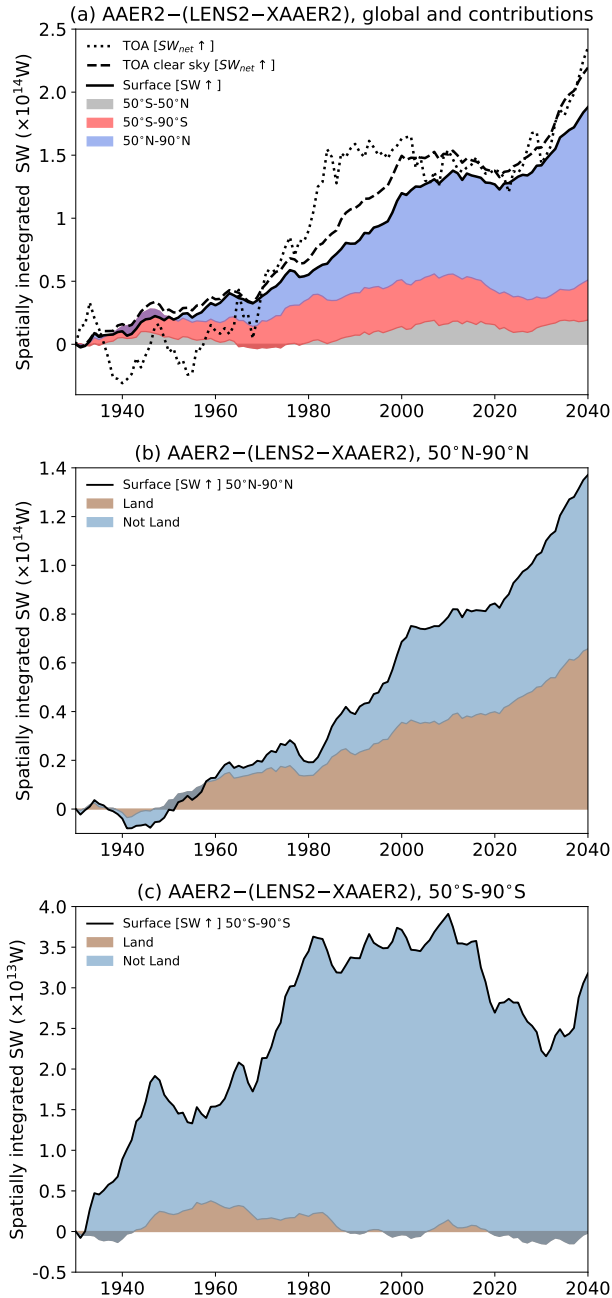
---

<sup>1</sup>An aside is that in Fig. 3d, LENS2–XAAER2 is the odd one out, with AAER1, LENS1–XAAER1 and AAER2 all exhibiting similar changes in [ $LW_{net} \uparrow$ ]. This may appear at odds with the fact that it is AAER2 that exhibits a different temperature response (Fig. 3b). The reason why AAER1 and LENS1–XAAER1 exhibit a greater decline in TOA [ $LW_{net} \uparrow$ ] than LENS2–XAAER2, even though their temperature responses are similar is actually because of cloud longwave radiative effects. Examination of clear sky [ $LW_{net} \uparrow$ ] (supplemental Fig. 5) reveals what we expect: AAER1, LENS1–AAER1 and LENS2–XAAER2 which all cool less than AAER2, also exhibit a smaller decline in clear sky [ $LW_{net} \uparrow$ ].

464 as surface [ $SW \downarrow$ ] declines, because a larger proportion is being reflected back to the atmosphere,  
465 and ultimately to space.

466 The difference in surface [ $SW \uparrow$ ] between AAER2 and LENS2–XAAER2 (solid in Fig. 5a)  
467 explains most of the difference in TOA clear sky (dashed in Fig. 5a) and TOA all sky [ $SW_{net} \uparrow$ ]  
468 (dotted in Fig. 5a). Consideration of how the surface shortwave albedo varies as a function of  
469 [AOD] (Fig. 4f) and [ $T_s$ ] (Fig. 4g) reveals that there is a systematic difference between the “all-  
470 but-one” and “only” approach in both CESM1 and CESM2. For [ $T_s$ ] anomalies down to around  
471  $-0.3\text{K}$  and [AOD] anomalies up to about  $5 \times 10^{-3}$  the albedo increases more for the “only” approach  
472 than for the “all-but-one” approach. But then, beyond that, the difference in behavior of the albedo  
473 between AAER2 and LENS2–XAAER2 increases rather dramatically. In the late 20th century,  
474 the surface shortwave albedo continues to increase in AAER2 (Fig. 3h), but in LENS2–XAAER2  
475 the albedo increase levels off at a much lower value and then starts to decline. This is apparent as  
476 a rather dramatic difference between AAER2 and LENS2–XAAER2 in the relationship between  
477 surface shortwave albedo and both [AOD] and [ $T_s$ ] (Figs. 4 f and g). In AAER2, as the planet  
478 cools, surface shortwave albedo keeps on increasing, presumably providing a positive feedback  
479 onto the cooling (Fig. 4g). In LENS2–XAAER2, as the planet cools, albedo also increases, but  
480 to a lesser extent, and then in the 1990s, albedo starts to decline and the planet begins to warm up  
481 again, even though the [AOD] has continued to increase.

488 Increased surface shortwave albedo generates cooler temperatures and vice versa, so separating  
489 out cause and effect is challenging in these quasi-equilibrium experiments where the system has  
490 adjusted to a new balance. Nevertheless, given that there is no evidence that the origins of the  
491 different [ $T_s$ ] response between AAER2 and LENS2–XAAER2 lies in differences in how the  
492 incoming surface shortwave radiation behaves, we posit that it lies in non-linearity in surface  
493 shortwave albedo feedbacks and that there are two components that contribute to this shortwave  
494 albedo non-linearity, which will now be discussed: (1) a non-linearity in both snow and sea ice  
495 albedo feedbacks and; (2) a non-linearity related to the North Atlantic ocean circulation which  
496 leads to differing northward heat transport into the Arctic and associated differences in high  
497 latitude albedo. In the following sub-sections we provide the evidence for both of these sources of  
498 non-linearity in surface shortwave albedo.



482 FIG. 5. Difference between AAER2 and LENS2-XAAER2 in the spatially integrated shortwave fluxes. (a) shows the global  
 483 integral with black dotted showing the top of atmosphere net upward shortwave radiation and black dashed showing its clear sky  
 484 component. Black solid shows the surface upward shortwave radiation and it is further divided into contributions from different  
 485 latitude bands. (b) Surface upward shortwave radiation spatially integrated from 50°N to 90°N and the contributions from land  
 486 regions and regions that are not land. (c) is as (b) but for 50°S to 90°S. Note the differing magnitudes covered by the y axes in (b)  
 487 and (c).

499 *b. Albedo non-linearities*

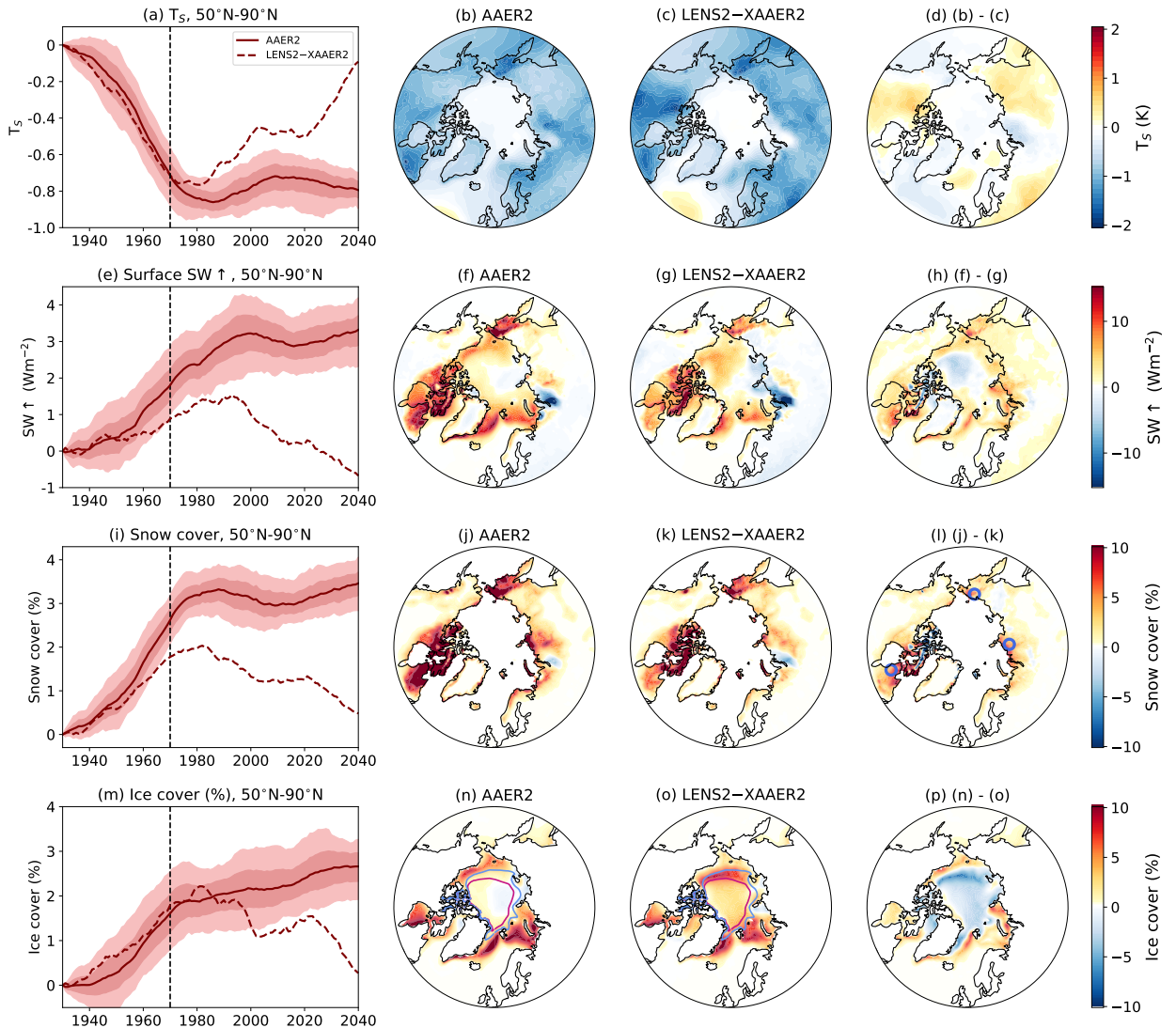
500 1) SNOW AND SEA ICE NON-LINEARITIES

501 Figure 5a shows the spatially integrated difference in the surface upward shortwave radiation,  
 502 [SW ↑] between AAER2 and LENS2-XAAER2 (solid black) and this difference is further de-

503 composed into the contribution from different latitude bands. The high latitudes (poleward of 50°  
504 latitude) clearly dominate in this difference. Both SH (salmon) and NH (blue) play a role, but the  
505 NH difference in surface  $SW \uparrow$  dominates in the late 20th and 21st centuries. This difference in  
506 surface  $SW \uparrow$  between AAER2 and LENS2–XAAER2 in the high latitudes of each hemisphere can  
507 be further decomposed into the contribution from land regions and the contribution from “not land”  
508 regions, i.e., regions that are either ocean or sea ice. In the NH, the land and not land contribute  
509 roughly equally to the difference between AAER2 and LENS2–XAAER2 from the 2000s onward  
510 (Fig. 5b) and the difference over land regions dominates prior to that. In the SH, the difference  
511 over ocean and sea ice regions dominates (Fig. 5c).

512 A seasonal decomposition of the difference in surface  $SW \uparrow$  integrated over 50°N to 90°N between  
513 AAER2 and LENS2–XAAER2 indicates the summer season as dominating in the  $SW \uparrow$  difference  
514 initially (supplemental Fig. 6), which makes sense given that this is when there is the greatest  
515 incident shortwave radiation which can then be affected by differences in surface shortwave albedo  
516 feedbacks. Later in the simulation, differences in  $SW \uparrow$  between the methods becomes increasingly  
517 important in the shoulder seasons as well. In order to understand the origins of this difference in  
518 surface shortwave albedo behavior we now focus on the NH during summer (June-July-August,  
519 JJA).

520 Consider the time series of 21-year running mean JJA 50°N-90°N  $T_s$  shown in Fig. 6a. This  
521 shows that NH high latitude temperature declines at a similar rate in AAER2 and LENS2–XAAER2  
522 until around 1960-1980, at which point LENS2–XAAER2 starts to warm, while AAER2 does not.  
523 We consider the behavior of surface  $SW \uparrow$ , snow cover and sea ice cover during the 1960-1980  
524 average in an attempt to examine their differences before subsequent feedbacks associated with  
525 the differing  $T_s$  response are present. For 50°N-90°N average surface  $SW \uparrow$ , a difference between  
526 AAER2 and LENS2–XAAER2 is already apparent during 1960-1980, even though a difference in  
527  $T_s$  is not (see Fig. 6b-d for local temperature changes). It is clear from Figs. 6 f-h that in AAER2,  
528 there is a greater enhancement in surface  $SW \uparrow$  around the sea ice edge and over high latitude land  
529 regions than in LENS2–XAAER2. There is also less of an increase in surface  $SW \uparrow$  in the interior  
530 regions of the sea ice in AAER2 compared to LENS2–XAAER2, leading to a difference in  $SW \uparrow$   
531 between the methods that is negative there. These differences in  $SW \uparrow$  correspond reasonably well  
532 to differences in sea ice cover between AAER2 and LENS2–XAAER2 (Fig. 6n-p).



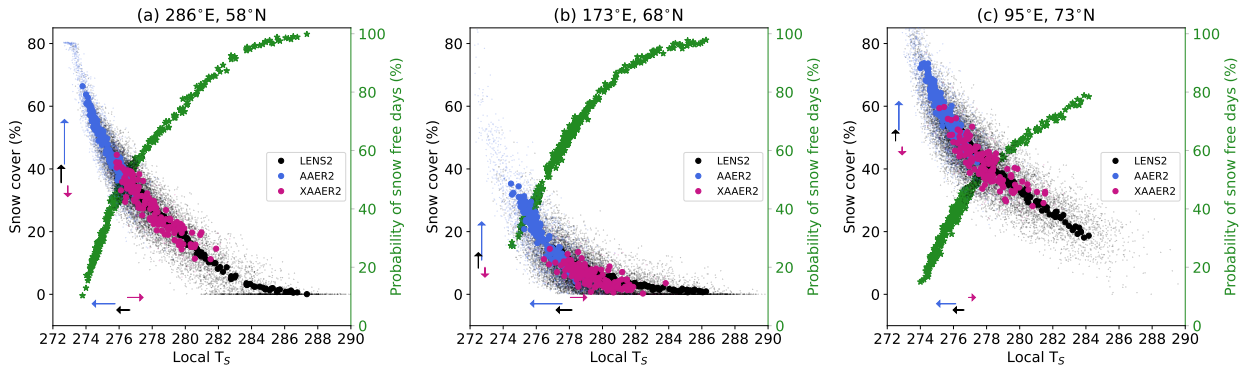
533 FIG. 6. Aerosol influence on the JJA season from 50°N to 90°N. Left column shows time series of 21-year running means for (solid) the ensemble mean of AAER2 and (dashed) the ensemble mean of LENS2-XAAER2 anomalies from the 1920-1940  
 534 for (solid) the ensemble mean of AAER2 and (dashed) the ensemble mean of LENS2-XAAER2 anomalies from the 1920-1940  
 535 average. The dark and light shadings around the AAER2 line show the 95% confidence interval using (light shading) 3 members  
 536 and (dark shading) 15 members. The dashed vertical line depicts the 21-year mean centered on 1970, i.e., the 1960-1980 average  
 537 shown in the right three columns. (2nd column) shows 1960-1980 anomalies compared to 1920-1940 for AAER2, (3rd column)  
 538 is as (2nd column) but for LENS2-XAAER2 and (4th column) shows the difference in the anomalies between AAER2 and  
 539 LENS2-XAAER2. (top)  $T_s$ , (2nd row) surface upward shortwave, (3rd row) grid cell area covered by snow in percent, (4th row)  
 540 grid cell area covered in sea ice in percent. In (i) and (m) the 50°N-90°N average is taken only over land grid points and grid points  
 541 that are not land, respectively. Blue points in (l) show the grid points used for the analysis in Fig. 7 ( (286°E,58°N), (173°E,68°N),  
 542 (95°E,73°N) ). The blue and pink contours in (n) and (o) show the 80% sea ice contours for 1920-1940 of AAER2 and 1960-1980  
 543 of XAAER2, respectively.

544 Over the NH land regions surrounding the Arctic, there is a greater increase in summer snow  
 545 cover in AAER2 than in LENS2-XAAER2 (Fig. 6l) corresponding well to regions where the  
 546 difference in surface  $SW \uparrow$  is largest over land. Figure 7 demonstrates that snow cover fraction

547 depends non-linearly on local temperature at three representative locations, given by the blue  
548 circles in Fig. 6l: a grid point to the east of Hudson Bay; one in Eastern Siberia; and one to the  
549 south of the Kara Sea. Specifically, a cooling/warming that occurs at a lower temperature would  
550 be associated with a larger increase/decrease in snow cover than if that same cooling/warming  
551 occurred at a higher temperature. This can be understood as a result of snow cover being bounded  
552 by zero. For warmer temperatures, there is a higher probability of there not being snow on the  
553 ground (green stars in Fig. 7) and for times when there is no snow on the ground a further warming  
554 can no longer lead to a change in snow cover, leading to a weaker dependence of seasonal average  
555 snow cover on temperature at warmer temperatures. The arrows in Fig. 7 help to illustrate this  
556 non-linearity by showing the 1920-1940 average at the start point of the arrow and the 1960-1980  
557 average at the end point of the arrow. For the change that is inferred to be due to the aerosol forcing,  
558 the cooling in AAER2 which has a colder starting point, leads to a proportionately larger increase  
559 in snow cover than the cooling in LENS2 does and both lead to a proportionately larger change in  
560 snow cover than the warming in XAAER2, which is warming rather than cooling. The result is  
561 that the magnitude of the increase in snow cover in AAER2 (given by the length of the blue arrow)  
562 is proportionately larger for the temperature change than that in LENS2–XAAER2 (given by the  
563 sum of the black and the pink arrow lengths). This effect is likely what dominates prior to 1980  
564 in the differences seen between the methods in the NH, given the dominance of land regions in  
565 contributing to the SW↑ differences (Fig. 5b).

576 For sea ice, both AAER2 and LENS2–XAAER2 exhibit an increase in sea ice cover, but they  
577 do so at different locations - the increase in AAER2 (Fig. 6n) is generally at lower latitudes than  
578 the increase in LENS2–XAAER2 (Fig. 6o). The reason for this is fairly straightforward - in  
579 AAER2, the cooling is occurring relative to a cold climate (a pre-industrial climate which has then  
580 cooled slightly under aerosol forcing out to the baseline 1920 to 1940 period), while in LENS2  
581 compared to XAAER2, the aerosol influence is felt relative to a climate in which sea ice has been  
582 influenced by greenhouse gas driven warming. To illustrate the differing sea ice fractions between  
583 the different baseline climates that the aerosol influence is being compared against in Fig. 6, we  
584 show the 80% sea ice fraction contours for the 1920-1940 climate of AAER2 in blue and for the  
585 1960 to 1980 climate of XAAER2 in pink in panels n and o. The 1920-1940 climate is the baseline  
586 for AAER2. For the “all-but-one” method, the baseline climate is more complicated but since





566 FIG. 7. Evolution of snow cover as a function of local  $T_s$  for the three points shown in Fig. 6l: (a) 286°E, 58°N (east of Hudson  
 567 Bay); (b) 173°E, 68°N (eastern Siberia); and, (c) 95°E, 73°N (south of the Kara Sea). Dots show the JJA seasonal mean percentage  
 568 of the grid point covered by snow versus local  $T_s$ . Small dots show the individual seasons for all members and all years and large  
 569 dots show the ensemble means for each year. Blue = AAER2, pink = XAAER2 and black = LENS2 (LENS2 is shown out to 2100).  
 570 The green stars (right axis) show the probability of snow free days in the JJA season assessed for each year by pooling together all  
 571 members from either LENS2 or AAER2 (XAAER2 is not shown for this metric given its smaller ensemble size). The start point  
 572 of each of the arrows shows the ensemble mean 1920-1940 average value and the end point shows the ensemble mean 1960-1980  
 573 average. The overall change in AAER2 is simply quantified by the length and direction of the blue arrow while the magnitude of the  
 574 change in LENS2–XAAER2 is given by summing up the length of the black and pink arrows when they are in opposite directions,  
 575 as in all cases here and the direction of change is that of the black arrow.

587 we are comparing the 1960-1980 minus 1920-1940 anomalies of LENS2 with that in XAAER2,  
 588 and the sea ice fraction doesn't differ substantially between LENS2 and XAAER2 in 1920-1940  
 589 (not shown), the baseline for the aerosol influence in LENS2–XAAER2 is effectively 1960-1980  
 590 of XAAER2. The 80% sea ice fraction metric indicates that a high sea ice fraction is present  
 591 for a wider latitude range in the colder AAER2 climate and, as a result, the additional growth  
 592 due to the anthropogenic aerosol influence occurs at lower latitudes compared to the growth that  
 593 occurs in LENS2 relative to XAAER2. Note that the difference in ice fractions between 1920-1940  
 594 of AAER2 and 1960-1980 of XAAER2 is also accompanied by differences in sea ice thickness  
 595 (thicker ice in the central Arctic in AAER2) which will also impact on where additional sea ice  
 596 under aerosol-forced cooling will grow. The overall result is that AAER2 gains more sea ice at  
 597 low latitudes and less sea ice at high latitudes compared to LENS2–XAAER2 (Fig. 6p). While  
 598 the latitude at which sea ice is gained under aerosol forcing clearly represents a state dependence  
 599 leading to differences between the methods, its effects on  $SW\uparrow$  during the summer months is likely  
 600 small, given that during the summer, the latitudinal gradients in incoming shortwave are small.  
 601 But this could be a contributor to the method dependence of  $SW\uparrow$  anomalies during the spring  
 602 and autumn, when insolation is relatively greater at lower latitudes. In addition to this difference  
 603 in latitude at which sea ice is gained, supplemental Fig. 7 shows the dependence of JJA averaged

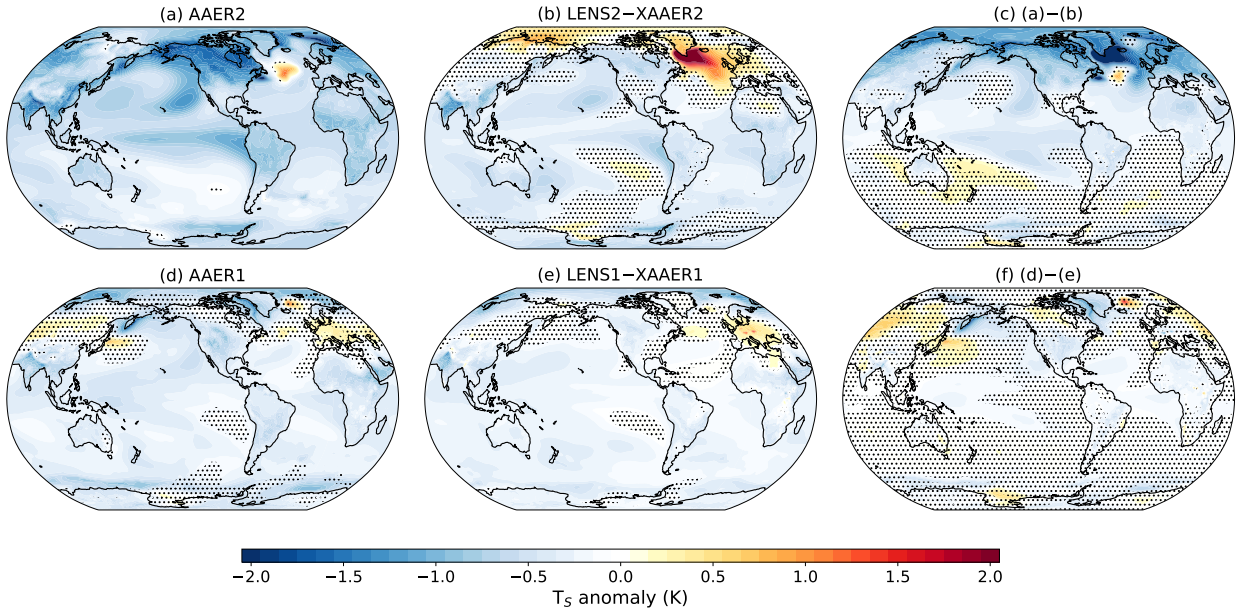
604 sea ice fraction on temperature, in a similar manner to Fig. 7 for snow, where it can be seen that a  
605 non-linearity is also present in association with sea ice being bounded by zero and, therefore, the  
606 probability of having days with zero sea ice increases with increasing temperature.

607 In the SH, summer sea ice fraction differences and their relation to differences in surface upward  
608 shortwave radiation are also clear. AAER2 shows greater increases in sea ice cover overall with a  
609 strong correspondence between regions where sea ice has increased more and regions where the  
610 increase in upward shortwave from the surface is greater (supplemental Fig. 8).

611 In summary, the behavior of snow cover and sea ice and their influence on surface upward  
612 shortwave radiation appear to be state dependent, i.e., it matters whether aerosol forcing is imposed  
613 within a cold pre-industrial climate or whether it is imposed within a climate state that has also  
614 experienced greenhouse gas forcing. An aerosol cooling that occurs at a colder temperature, as in  
615 AAER2, increases the average snow cover more than an aerosol induced cooling that occurs within  
616 a planet that has warmed under greenhouse gas forcing, as in LENS2 compared to XAAER2.  
617 The same is true for sea ice and, in addition, sea ice that is gained during the cooling of a colder  
618 climate tends to occur at lower latitudes than the sea ice gains that occur during the cooling of a  
619 warmer climate. These snow cover and sea ice non-linearities lead to an overall larger influence  
620 on shortwave radiation for the colder base state in AAER2.

## 621 2) THE NORTH ATLANTIC OCEAN CIRCULATION

622 The annual mean  $T_s$  response to anthropogenic aerosol forcing by 2030-2050 can be seen in Fig.  
623 8. By this time period, AAER2 (Fig. 8a) is colder than LENS2–XAAER2 (Fig. 8b) over much  
624 of the globe, with the largest differences found in the NH high latitudes, over continental regions,  
625 around the margins of Antarctic sea ice and in the tropical and sub-tropical Pacific (Fig. 8c). The  
626 fact that the  $T_s$  differences extend beyond the high latitudes is not inconsistent with the important  
627 role for high latitude feedbacks in producing them because similar anomalies, with opposite sign  
628 relative to those in Fig. 8c in the tropical Pacific have been found in response to sea ice loss (as  
629 opposed to gain in our case) (Deser et al. 2015) with an important role for ocean dynamics in  
630 transferring the signal there (Wang et al. 2018).



638 FIG. 8. Differences in annual mean  $T_s$  between 2030-2050 and 1920-1940. (a)-(c) CESM2 AAER2, LENS2-XAAER2 and  
 639 the difference between them. (d)-(f) as (a)-(c) but for CESM1. Stippling indicates anomalies that are not statistically significant at  
 640 the 95% confidence level.

631 Consideration of the differences between AAER2 and LENS2-XAAER2 in 2030-2050, however,  
 632 reveals another important feature: there is a clear difference in the sub-polar North Atlantic with a  
 633 substantial warm anomaly in the region south of Greenland in LENS2-XAAER2 (Fig. 8b), which  
 634 is much less apparent in AAER2 (Fig. 8a). In LENS2-XAAER2, there is also a warm anomaly  
 635 over much of the Arctic. It is clear that there are large differences between the two methods in the  
 636  $T_s$  response over the NH high latitudes and in the sub-polar gyre region to the south of Greenland,  
 637 in particular (Fig. 8c), while the same method-dependence is not found in CESM1 (Fig. 8d-f).

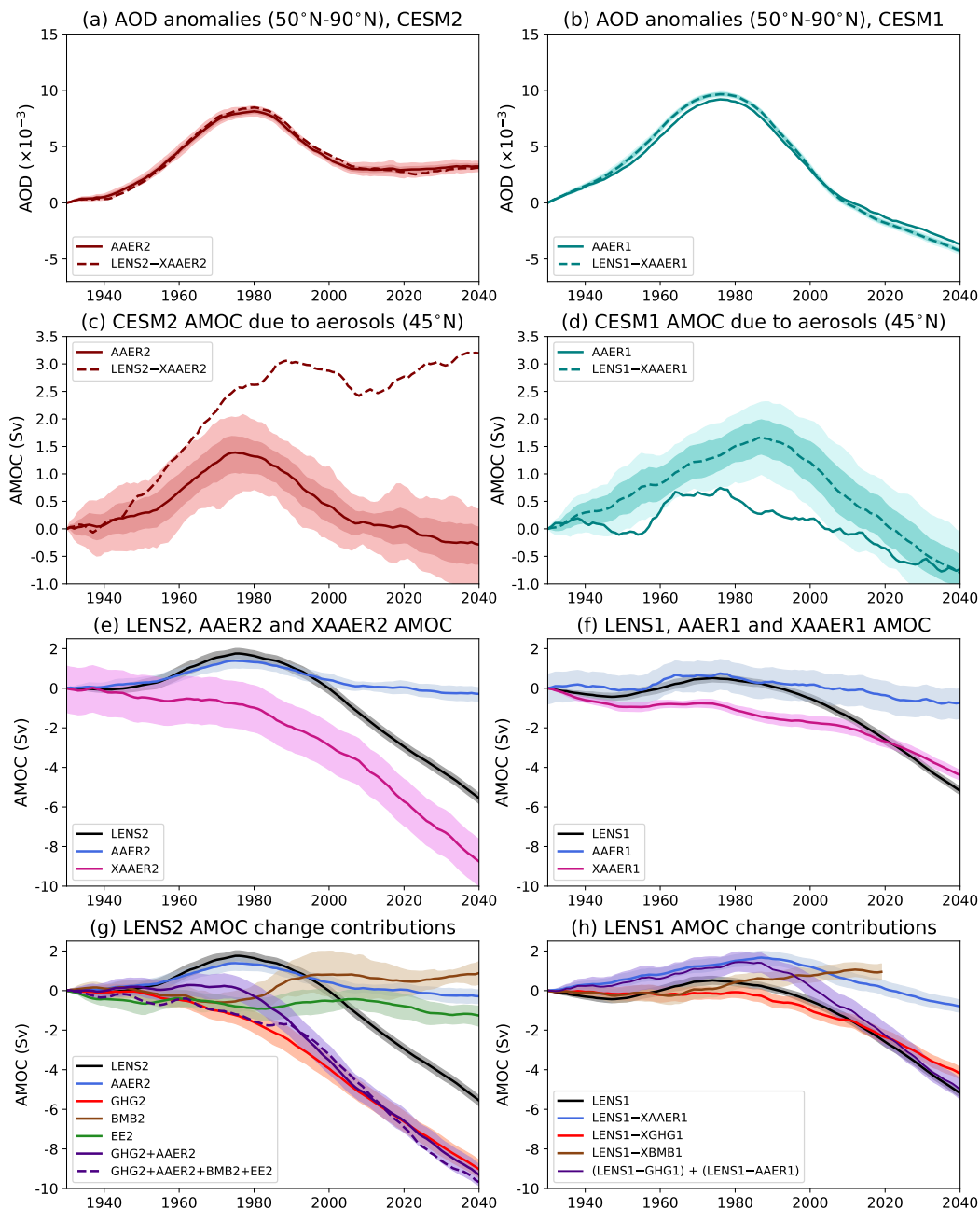
641 The warm sub-polar gyre  $T_s$  anomaly in LENS2-XAAER2 to the south of Greenland resembles  
 642 what would be expected from a strengthening of the AMOC (e.g., Delworth et al. 2017). Indeed,  
 643 consideration of the AMOC response, defined as the change in the magnitude of the maximum  
 644 meridional overturning streamfunction at  $45^\circ\text{N}$  below 500 m depth, reveals a strong dependency  
 645 of the aerosol-forced AMOC changes on the experimental design in CESM2 (Fig. 9c).

646 First, it is worth considering how the NH aerosol forcing evolves as this is likely to be more  
 647 directly connected to forcing of AMOC changes than the global mean aerosol evolution. Figure  
 648 9a shows that the  $50^\circ\text{N}$  to  $90^\circ\text{N}$  AOD in CESM2 increases to a maximum in the 1970s and 1980s  
 649 and then declines but levels off at higher AOD values than the 1920-1940 period for the remainder

650 of the simulation. In AAER2, the AMOC increases in strength to a maximum in the 1970s and  
651 then declines (Fig. 9c, solid), somewhat following the NH high latitude aerosol forcing, except it  
652 returns to the baseline AMOC strength despite the positive AOD anomalies in the 21st century.  
653 In contrast, the AMOC in LENS2–XAAER2 increases in strength more rapidly and then, rather  
654 than decreasing with the decline in aerosol forcing, it plateaus and even slightly increases out to  
655 the end of the simulation (Fig. 9c, dashed). Consideration of XAAER2 in isolation (pink in Fig.  
656 9e) reveals that as the planet warms in the absence of aerosol forcing and the presence of rising  
657 greenhouse gases, the AMOC in CESM2 starts to decline rapidly around 1980. This is rather  
658 similar to what is seen in GHG2 (red in Fig. 9g). In contrast, in LENS2 when all forcings are  
659 present, the anthropogenic aerosol forcing seems to dominate and acts to strengthen the AMOC  
660 until about 1980, delaying this rapid greenhouse gas-forced decline in AMOC until later in the  
661 simulation (black in Figs. 9e and g). The result is a non-linear behavior of AMOC in the CESM2  
662 simulations with the sum of the individual forcing contributions not adding up to the LENS2  
663 response (compare black and dashed purple in Fig. 9g).

675 The LENS2 AMOC decline begins around 1980 but it does not fall below the 1920-1940 baseline  
676 until about 2000 and at that point it declines at a rather similar rate to what was seen earlier in  
677 XAAER2. The AMOC in XAAER2 starts to decline very rapidly around 1980, and because the  
678 aerosols in LENS2 delay the onset of this rapid decline compared to XAAER2, the aerosol influence  
679 inferred from LENS2–XAAER2 is an apparently greater strengthening of the AMOC than that  
680 inferred when the aerosols are imposed in isolation in AAER2. It is not that the aerosol forcing  
681 by itself produces the strengthening inferred from LENS2–XAAER2, but it is that it staves off the  
682 rapid greenhouse gas-forced AMOC decline. This can explain the warm anomalies in the NH high  
683 latitudes and the sub-polar North Atlantic due to aerosol forcing estimated from LENS2–XAAER  
684 in Fig. 8b, whereas in AAER2, the AMOC strengthening is weaker and declines after the 1980s.  
685 The increased AMOC strength in LENS2–XAAER2 leads to enhanced northward ocean heat  
686 transport into the NH high latitudes (not shown), which is a further boost to the disparity in surface  
687 albedo between the two methods through effects on sea ice and snow melt.

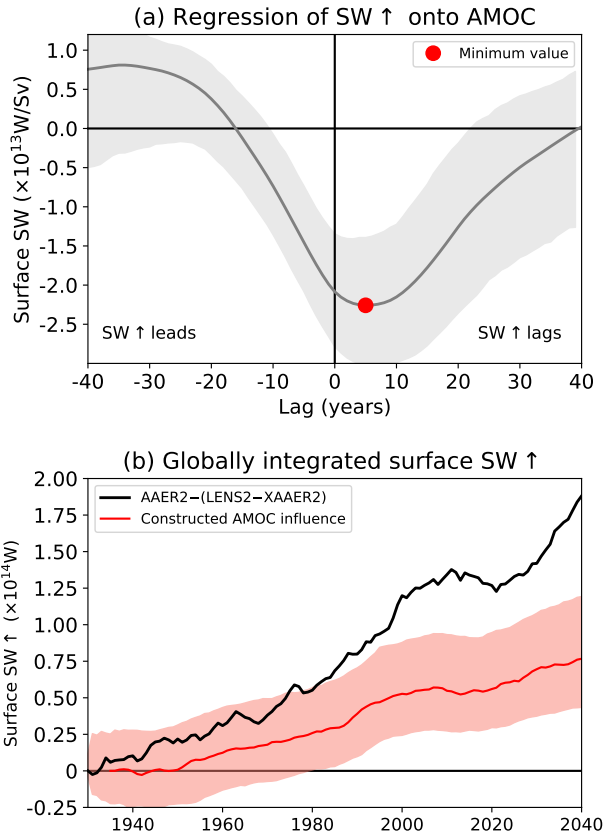
688 It is challenging to truly isolate the relative importance of AMOC versus the other albedo non-  
689 linearities described above to the method-dependence of the global surface upward shortwave  
690 radiation, but we can at least obtain a rough estimate of the order of magnitude of AMOC's



664 FIG. 9. (a) and (b) 21-year running mean AOD anomalies (relative to 1920 to 1940) averaged from 50°N to 90°N for CESM2 and  
 665 CESM1 anthropogenic aerosol forcing, respectively. The remaining panels show 21-year running mean AMOC anomalies (relative  
 666 to 1920 to 1940) where AMOC is defined as the magnitude of the maximum meridional overturning streamfunction below 500m  
 667 depth in the North Atlantic at 45°N. (c) and (d) show the inferred AMOC changes due to anthropogenic aerosol forcing using both  
 668 methods for CESM2 and CESM1, respectively, with 95% confidence intervals provided for AAER2 in (c) and LENS1–XAAER2  
 669 in (d) using 3 members (light) and the number of members in the large ensemble (dark). (e) and (f) show the AMOC anomalies  
 670 for all forcings, the AAER simulation and the XAAER simulation for CESM2 and CESM1, respectively. (g) and (h) show the  
 671 decomposition of the overall change in AMOC in the large ensemble into the contributions that are inferred to be due to individual  
 672 forcings for CESM2 and CESM1, respectively. 95% confidence intervals on the ensemble means are shown in (e)–(h). For the 3  
 673 member XAAER2 and AAER1 ensembles in (e) and (f), respectively, the 95% confidence interval is calculated by bootstrapping  
 674 the pre-industrial control.

691 impacts by considering the association of globally integrated surface upward shortwave radiation  
692 with AMOC variability in the CESM2 pre-industrial control simulation. Figure 10a shows the  
693 regression of 21-year running mean globally integrated surface SW $\uparrow$  anomalies onto AMOC (after  
694 linearly detrending to remove the pre-industrial control drift). This shows that following an increase  
695 in AMOC of 1Sv, the globally integrated surface SW $\uparrow$  declines by just under  $2.5 \times 10^{13}$ W about  
696 5 years later. We then use this relationship between AMOC and globally integrated surface SW $\uparrow$   
697 with a lag of 5 years to construct the influence of the AMOC anomalies in each experiment on  
698 globally integrated surface SW $\uparrow$  and the difference in this between AAER2 and LENS2–XAAER2.  
699 A comparison of this constructed AMOC influence on surface SW $\uparrow$  with the difference in globally  
700 integrated surface SW $\uparrow$  between AAER2 and LENS2–XAAER2 suggests that the influence of  
701 the method-dependence on AMOC can explain a little under half of the influence of the method-  
702 dependence on the globally integrated surface upward SW $\uparrow$ , with presumably the other albedo  
703 effects described above contributing to the remainder (Fig. 10b). This assumes that we can linearly  
704 relate globally integrated SW $\uparrow$  to AMOC variability and that there is no dependence of AMOC-  
705 related surface upward shortwave variability on the climate base state. An analysis of similar  
706 regressions to those in Fig. 10a throughout the transient LENS2 simulations suggests that it is,  
707 indeed, a reasonable approximation to assume that the piControl regression of SW $\uparrow$  onto AMOC  
708 is representative of that over the 20th and early 21st centuries (Supplemental Fig. 9).

722 A variety of processes can force an AMOC decline under climate change, including reduced  
723 sensible heat loss from the ocean in the presence of a warmer atmosphere (Weaver et al. 2007;  
724 Brodeau and Koenigk 2016), altered freshwater forcing as precipitation and evaporation patterns  
725 change (Manabe and Stouffer 1993; Dixon et al. 1999) and altered lateral transports of freshwater  
726 into regions of deep convection as a result of sea ice loss (or melting of the Greenland Ice Sheet,  
727 although Greenland ice sheet melt is not represented in these CESM2 simulations) (Jahn and  
728 Holland 2013; Yang et al. 2016; Li et al. 2021). Once an AMOC decline has been induced, positive  
729 feedbacks, particularly from the reduced advection of salty water from southern latitudes, can  
730 further enhance the AMOC decline. Such feedbacks have also been argued recently by Hassan  
731 et al. (2021) and Robson et al. (2022) to be important in the aerosol-forced strengthening of AMOC.  
732 A more detailed analysis of the reasons behind the substantial AMOC decline under GHG forcing  
733 in CESM2 is warranted and, while we leave this for future work, we provide a cursory assessment



709 FIG. 10. (a) Regression of 21-year running mean globally integrated surface upward shortwave radiation onto 21-year running  
 710 mean AMOC strength, defined as the maximum streamfunction below 500 m at 45°N, in the CESM2 pre-industrial control. The  
 711 gray shaded range shows a 95% confidence interval determined by bootstrapping with replacement 200-year segments of the  
 712 pre-industrial control, concatenating them to obtain 1000 time series of equivalent length to the 1600-year pre-industrial control  
 713 simulation, recalculating the regression and obtaining the 2.5th to 97.5th percentile range. The red point marks the minimum  
 714 value of this regression curve. (b) Black shows the time series of the difference between AAER2 and LENS2-XAAER2 21-year  
 715 running mean globally integrated surface upward shortwave (reproduced from Fig. 5a) and red shows the estimated influence of the  
 716 difference in AMOC changes between AAER2 and LENS2-XAAER2 by constructing the AMOC influence on globally integrated  
 717 surface SW $\uparrow$  by  $-2.26e13 \cdot \text{AMOC}(t-5)$  where  $-2.26e13$  is the minimum regression coefficient in panel (a) and occurs at a lag of 5  
 718 years and AMOC refers to the annual mean AMOC strength anomalies relative to 1920-1940 using the maximum streamfunction  
 719 below 500m at 45°N definition for AMOC strength. The uncertainty range on this construction is determined by recalculating the  
 720 construction using the bootstrapped minimum regression coefficients and lags that were used to determine the confidence interval  
 721 in panel (a) and obtaining the 2.5th to 97.5th percentile range of these bootstrapped constructions.

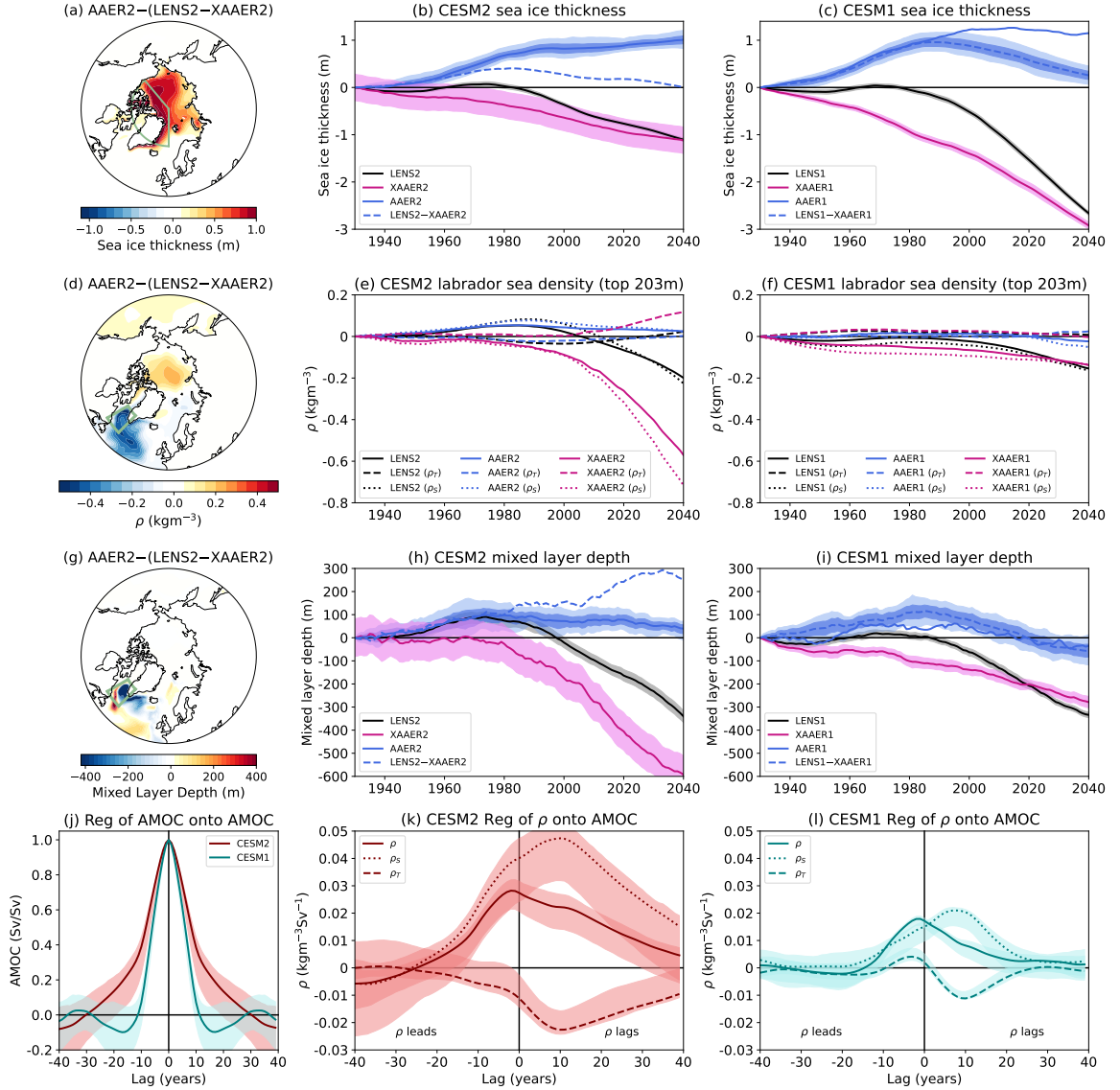
734 of the different forcing factors that could lead to an AMOC decline for the XAAER2 simulation  
 735 in supplemental Fig. 10 to shed some light on the possible causes of the AMOC declines shown  
 736 in Fig. 9e and g. This suggests that the freshwater input associated with sea ice loss is the most  
 737 likely candidate forcing of the AMOC decline. The annual mean sea ice thickness anomalies are  
 738 also shown in Fig. 11b and this shows that the Arctic sea ice thickness declines occur earlier in  
 739 the absence of aerosol forcing (compare pink and black lines in Fig. 11b). This freshwater forcing  
 740 likely leads to a decline in the near surface density of sea water ( $\rho$ ) in the Labrador Sea through

741 a reduction in salinity, as quantified for March in Fig. 11e. Here,  $\rho$  anomalies averaged over the  
742 top 203m of the ocean in the Labrador Sea have been decomposed into the parts associated with  
743 salinity ( $\rho_S$ ) and temperature ( $\rho_T$ ) using an equation of state for sea water (McDougall et al. 2003),  
744 and the salinity component is dominating. Associated with this is a reduction in convection in the  
745 Labrador Sea, as depicted via the substantial reductions in March mixed layer depth in Fig. 11h,  
746 which uses the definition of Large et al. (1997).

747 We suspect, based on Fig. 11k that there is also an important role for positive salinity feedbacks  
748 in the rapid AMOC decline with greenhouse gas forcing in CESM2. Figure 11k shows the lagged  
749 regression of Labrador Sea density ( $\rho$ ,  $\rho_S$  and  $\rho_T$ ) anomalies onto AMOC in the CESM2 pre-  
750 industrial control simulation using 10-year running means. We switch to using 10-year running  
751 means here for consistency with the study of Danabasoglu et al. (2019) which made use of this  
752 metric to indicate the role of density anomalies in driving and feeding back onto AMOC anomalies.  
753 In the pre-industrial control variability, the maximum positive density anomalies due to changing  
754 salinity lag the AMOC (dotted in Fig. 11k). This dominates over temperature feedbacks to lead  
755 to an overall positive density feedback on AMOC variability. We also suspect that differences in  
756 this feedback between CESM2 and CESM1 are important in their differing AMOC behavior, to be  
757 discussed in section 5.

758 Overall, when anthropogenic aerosol forcing is imposed on its own, it leads to an increase in sea  
759 ice thickness (solid blue in Fig. 11b), a slight increase in Labrador Sea density through increased  
760 salinity (solid blue in Fig. 11e) and a slight increase in AMOC strength (solid blue in Fig. 9e).  
761 However, when the anthropogenic aerosol influence is inferred from LENS2–XAAER2, because  
762 the aerosols postpone the decline in sea ice thickness,  $\rho$ , mixed layer depth and AMOC in LENS2  
763 compared to XAAER2, they lead to an apparent continued increase in Labrador Sea mixed layer  
764 depth over the course of the simulation (Fig. 11h, blue dashed) and an increase in AMOC strength  
765 (Fig. 9c, maroon dashed). The increase in AMOC strength is associated with enhanced ocean heat  
766 transport into the NH high latitudes and, presumably in association with this, the sea ice thickness  
767 starts to decline (blue dashed in Fig. 11b), as does the reduction in global mean temperature (Fig.  
768 3b, maroon dashed).





769 FIG. 11. (a) The difference in annual mean sea ice thickness anomalies between AAER2 and LENS2–XAAER2 during  
770 2030–2050. (b) 21-year running mean CESM2 annual mean sea ice thickness anomalies (relative to 1920–1940) averaged over  
771 220°E–360°E, 70°N–90°N (green region in (a)) for LENS2 (black), XAAER2 (pink), AAER2 (blue), and LENS2–XAAER2 (blue  
772 dashed), (c) as (b) but for CESM1. For AAER2 in (b) and LENS2–XAAER2 in (c) 95% confidence intervals are shown for a  
773 3-member ensemble (light) and an ensemble of size equal to the one shown (dark) and for other experiments, the shading shows  
774 the 95% confidence interval for a sample size equal to that in the ensemble. (d)–(f) show March density anomalies averaged over  
775 the top 203 m of the ocean and the averaging region for (e) and (f) is the Labrador Sea (300°E–315°E, 53°N–65°N, green box in  
776 (d)). The LENS2–XAAER2 anomalies are not shown in (e) and (f) and instead the density anomalies in the other simulations are  
777 decomposed into the part that is associated with temperature ( $\rho_T$  dashed) and the part that is associated with salinity ( $\rho_S$  dotted).  
778 (g)–(i) are as (a)–(c) but for March mixed layer depth and the averaging in (h) and (i) is performed over the Labrador Sea. (j) lagged  
779 auto-regression of annual mean AMOC. (k) lagged regression of March Labrador Sea density anomalies (and its temperature and  
780 salinity components) in the top 203 m onto annual mean AMOC for CESM2. (l) as (k) but for CESM1. In (j)–(l) 10 year running  
781 means are used for consistency with Danabasoglu et al. (2019)

782 *c. Summary of method-dependence*

783 In this section we have investigated the dependence of the anthropogenic aerosol-forced [ $T_s$ ]  
784 response to the method used in CESM2 (AAER2 versus LENS2–XAAER2). The surface energy  
785 balance indicates that aerosol forcing leads to a bigger decline in net TOA shortwave in AAER2  
786 compared to LENS2–XAAER2 (Fig. 2c), which drives a bigger decline in global mean  $T_s$  and an  
787 associated compensating decline in net TOA longwave radiation. The method-dependence of the  
788 TOA net shortwave radiation can be further narrowed down to difference in the surface upward  
789 shortwave radiation (Fig. 3g) linked to a difference in the surface shortwave albedo response (Fig.  
790 3h).

791 We then discussed three potential sources of this albedo non-linearity. The first two are non-  
792 linearities or base state dependencies in the response of snow cover and sea ice fraction to  $T_s$   
793 change. Snow cover over the continental regions surrounding the Arctic declines non-linearly  
794 with warming. This is because the amount of time (in the summer at least) that is spent without  
795 any snow cover increases with warming and, as a result, the amount of time in which further  
796 warming can influence the snow cover declines. The result is that the aerosol-forced cooling that  
797 is imposed within a cooler climate in AAER2, leads to a larger increase in snow cover than the  
798 aerosol-forced cooling that is imposed within a warmer climate that is influenced by CO<sub>2</sub>, as is the  
799 case in the LENS2 versus XAAER2 comparison. Sea ice exhibits a similar non-linear behavior  
800 and there is also a dependence of the latitude at which sea ice grows with aerosol-forced cooling  
801 on the base state climate. In the cold climate within AAER2, additional sea ice grows at lower  
802 latitudes and while the impacts of this on the global radiative balance is likely minimal during the  
803 summer, it may matter more during the spring and autumn when latitudinal gradients in insolation  
804 are larger. These cryospheric effects lead to overall greater increases in albedo in AAER2 than  
805 in LENS2–XAAER2, and ultimately a differing global response as atmospheric and oceanic heat  
806 transports respond.

807 Finally, there is also clearly a non-linear behavior of AMOC which further widens the discrep-  
808 ancly between AAER2 and LENS2–XAAER2. In CESM2, with warming, the AMOC strength  
809 declines substantially and non-linearly. As a result, in LENS2 where aerosol forcing delays this  
810 AMOC decline, it leads to an apparently larger increase in AMOC strength due to aerosols in  
811 LENS2–XAAER2 than is found due to aerosol forcing alone in AAER2. The associated increased

812 heat transport into the NH high latitudes in LENS2–XAAER2 would further alter sea ice and snow  
813 cover with associated albedo changes.

## 814 **5. Comparison between CESM2 and CESM1**

815 We motivated the analysis in section 4 by aiming to determine the relative roles of the experimental  
816 design used, the model physics and the aerosol forcing in leading to the differing anthropogenic  
817 aerosol responses between CESM1 and CESM2. The results point to an important influence of the  
818 method in CESM2, but the same method-dependence was not found in CESM1. While the cooling  
819 due to anthropogenic aerosol forcing is greater in AAER1 than in LENS1–XAAER1 (solid versus  
820 dashed teal in Fig. 3b), the difference is much smaller than in CESM2. There are two potential  
821 reasons for this: (1) the model physics and dynamics in CESM1 is such that non-linearities are  
822 less important and (2) the fact that the imposed aerosol forcing declines more rapidly from the  
823 1980s (see the Appendix) may mean that CESM1 does not have as much of a chance for the  
824 non-linearities to lead to a big deviation between the methods. We cannot really explore the effect  
825 of (2) without simulations with CESM2 run under a lower aerosol emissions scenario and this  
826 would be a worthwhile avenue for future research to truly quantify the relative importance of these  
827 two factors. Nevertheless, differences between CESM1 and CESM2 do suggest that there is a role  
828 for model differences in leading to more non-linearity in CESM2 than in CESM1 and that it is not  
829 solely the difference in aerosol forcing that is responsible, as now discussed.

830 CESM1 exhibits much less of a difference in global upward surface shortwave between AAER1  
831 and (LENS1–XAAER1) in the NH than was found between AAER2 and (LENS2–XAAER2),  
832 although the SH difference is comparable (see supplemental Fig. 11, which is the equivalent of  
833 Fig. 6 but for CESM1). CESM1 does not exhibit as substantial a method-dependence for sea ice  
834 cover in the low latitudes of the Arctic or for snow cover over the continents surrounding the Arctic  
835 (supplemental Fig 12) but there are some similarities in the method-dependence for sea ice in the  
836 SH (supplemental Fig. 13). The differences between CESM1 and CESM2 in the NH can perhaps  
837 be traced back to two differences between the CESM1 and CESM2 climates. In CESM1, the Arctic  
838 sea ice is thicker and more expansive (supplemental Fig. 14 and DuVivier et al. (2020)). A result of  
839 the more expansive sea ice in CESM1 is that there may be less room for sea ice to grow in the aerosol  
840 only simulation before the continent is reached, limiting the differences in the extent to which the

841 sea ice fraction increases at lower latitudes in AAER1 compared to LENS1–XAAER1. The second  
842 factor that may be important is that CESM1 has reduced summertime snow cover compared to  
843 CESM2 in portions of the continental regions surrounding the Arctic, in particular regions adjacent  
844 to Hudson Bay and to the south of the Barents-Kara Sea (supplemental Fig. 14c), which likely  
845 makes those regions less non-linear in their snow cover response to temperature anomalies (recall  
846 Fig. 7). These regions correspond to those where the wintertime snow density has increased the  
847 most in CESM2 compared to CESM1 in response to updated snow density parameterizations (see  
848 Fig. 5 of Simpson et al. (2022)), which is likely playing a role.

849 Another important difference between CESM1 and CESM2 is in the behavior of AMOC.  
850 CESM1 does exhibit a method-dependence of the aerosol-forced AMOC response (Fig. 9d).  
851 In LENS1–XAAER1 the AMOC strengthens more than in AAER1 (dashed versus solid in Fig.  
852 9d) but this does not last for the full length of the simulation. The LENS1–XAAER1 AMOC  
853 strength starts to decline substantially after about 1990 whereas the LENS2–XAAER2 AMOC  
854 strengthening continues out to the end of the simulation (Fig. 9d versus c). This may be partly  
855 due to the differing forcings between CESM1 and CESM2, but comparison of Figs. 9e and f  
856 makes clear that the behavior of AMOC in the XAAER simulations (pink), where aerosols are  
857 not evolving and greenhouse gas forcing is the primary driver, also differs considerably between  
858 CESM1 and CESM2. In XAAER2, the AMOC declines much more rapidly after around 1980  
859 than in XAAER1 and so the aerosol-forced strengthening inferred from the LENS-XAAER calcu-  
860 lation is smaller during this period in CESM1 than in CESM2. Subsequently, when the aerosol  
861 forcing starts to decline in the NH high latitudes, because it actually goes negative compared to  
862 the 1920-1940 baseline in CESM1, the aerosol forcing and GHG forcing act together to produce  
863 a sharper decline in AMOC in LENS1 than in XAAER1 in the 21st century (Fig. 9f black versus  
864 pink). The differing AMOC behavior is likely part of the reason why the high latitudes warm a lot  
865 less in response to greenhouse gas forcing in GHG2 than in LENS1–XGHG1 (supplementary Fig.  
866 15). In CESM2, the greenhouse gas-forced decline in AMOC is greater than in CESM1, which  
867 reduces the northward heat transport into the high latitudes and reduces the warming there.

868 We speculate that an important factor in the differing AMOC responses between XAAER2 and  
869 XAAER1 is in the strength of salinity feedbacks. We can consider the AMOC decline to consist  
870 of two parts: (1) the forcing which leads to the decline in the first place, which we argued for

871 CESM2 above was most likely the freshwater input to the Labrador Sea from sea ice melt; and, (2)  
872 subsequent feedbacks which are triggered as the AMOC starts to decline, including the reduced  
873 advection of salty water from the low latitudes to the high latitudes. The various potential forcers  
874 of AMOC decline (surface freshwater flux, surface heat flux and sea ice loss) can be compared  
875 between CESM1 and CESM2 for the XAAER experiment in supplemental Fig. 10. For both  
876 CESM1 and CESM2, sea ice loss appears as the most likely forcer of AMOC decline as it is  
877 the only one which leads the AMOC decline as opposed to lags it. However, a difference in  
878 sea ice loss cannot explain the differences in AMOC decline between XAAER1 and XAAER2,  
879 because the sea ice loss is actually greater in XAAER1 than in XAAER2 (compare Figs. 11b  
880 and c), while the AMOC decline is greater in XAAER2. This suggests that the reason behind the  
881 difference in AMOC decline between XAAER1 and XAAER2 is more likely to be a difference  
882 in the feedbacks rather than in the initial forcing of AMOC decline. Figure 11j, which shows  
883 the lagged autoregression of AMOC onto itself within the pre-industrial control simulations of  
884 CESM1 and CESM2, demonstrates that the timescale of AMOC variability is longer in CESM2  
885 than in CESM1. We may reasonably expect that a longer timescale AMOC variability is either due  
886 to longer timescale forcing, whether that be through sea ice variability or surface flux variability,  
887 or due to stronger feedbacks onto AMOC variability which would lengthen the persistence of any  
888 anomalies induced by the various forcers. Comparison of the lagged regression of density onto  
889 AMOC in Figs. 11k and l shows that the salinity anomalies that lag AMOC in CESM1 are much  
890 smaller than in CESM2, i.e., per unit Sverdrup increase in AMOC strength, the lagged increase  
891 in Labrador Sea salinity is greater in CESM2, which would provide a greater feedback onto an  
892 AMOC change and, therefore, enhance the persistence of AMOC variability. This suggests that the  
893 positive salinity feedback onto AMOC anomalies may be stronger in CESM2 than in CESM1, for  
894 reasons that are currently unknown. This could lead to the more rapid AMOC decline in XAAER2,  
895 even though the freshwater input through sea ice loss is smaller. A more detailed analysis of the  
896 AMOC decline in both simulations should be performed in future work to fully understand these  
897 differences. The updates to the ocean model in CESM2 compared to CESM1 are relatively minimal,  
898 but include the representation of mixing effects of estuaries, enhanced mesoscale eddy diffusivity  
899 at depth, the use of prognostic chlorophyll for shortwave absorption, and the use of a salinity  
900 dependent freezing point (Danabasoglu et al. 2020). Whether the differences in AMOC behavior

901 can be attributed to these ocean model changes or the changes to the coupled system introduced  
902 through updates to the other components remains to be understood. Hassan et al. (2022) recently  
903 argued that models that exhibit a greater AMOC response to forcing may do so because of a larger  
904 feedback between the AMOC and cloud cover in the sub-polar North Atlantic. However, we find no  
905 evidence of a substantial feedback between the AMOC and sub-polar North Atlantic cloud cover in  
906 CESM2 through regression of total cloud cover onto AMOC in the CESM2 pre-industrial control  
907 simulation (not shown).

908 Overall, the comparison of the behavior of CESM1 and CESM2 makes clear that even though the  
909 single forcing experimental design matters within CESM2, it probably does so because of particular  
910 features of both the representation of processes within the model and the imposed forcing.

## 911 **6. Discussion and Conclusions**

912 The implicit assumption when using single forcing experiments to attribute changes to individual  
913 forcings is that non-linearities are negligible. As discussed in the introduction, prior studies have  
914 drawn mixed conclusions as to whether non-linearities are important. Some of the studies with  
915 older model generations, e.g., Feichter et al. (2004) and Ming and Ramaswamy (2009), used a  
916 slab ocean, so any non-linearity related to AMOC would have been absent. The more recent  
917 study of Deng et al. (2020) is the most relevant to the results presented here since they explored  
918 non-linearity within coupled CESM1 time-slice simulations. They did not find substantial non-  
919 linearities in GMST and TOA radiative fluxes, aligned with our findings that the “only” versus  
920 “all-but-one” method does not dramatically alter those responses to aerosol forcing in transient  
921 experiments with CESM1. Further probing of other features by Deng et al. (2020) did reveal other  
922 non-linearities, specifically in September-November Arctic sea ice decline and in summertime  
923 precipitation over East Asia. The sense of their sea ice non-linearity was that when greenhouse  
924 gases and aerosols were imposed together, there was less sea ice decline than summing up the  
925 contributions from greenhouse gases and aerosols separately, which is the opposite of what we find  
926 for CESM2.

927 The considerable non-linearities that we infer in CESM2 from the difference between the “only”  
928 and “all-but-one” methods for anthropogenic aerosols and comparison to the behavior in CESM1  
929 and these other previous studies makes clear that non-linearities in the response to forcings can

930 be highly dependent on the model physics and/or the forcings used. Indeed Menary et al. (2020)  
931 find that in CMIP6 models in general, the aerosol and greenhouse gas-forced AMOC anomalies  
932 do approximately sum up to the response when all forcings are applied together. CESM2 is clearly  
933 a more non-linear model than CESM1, particularly when it comes to the AMOC response to  
934 forcings, but also likely in the impact of surface shortwave albedo feedbacks. For the sea ice  
935 aspects, the version of CESM2 used here is known to be deficient in its representation of sea ice  
936 (DuVivier et al. 2020) so sea ice changes should be interpreted with caution. For snow cover,  
937 further investigation is required to determine whether summertime snow cover in CESM2 is more  
938 aligned with observations than CESM1 (supplemental Fig. 14a-c), although Wieder et al. (2022)  
939 indicate that CESM2 does have too much snow water equivalent in the springtime in the regions  
940 adjacent to Hudson Bay and to the south of the Kara Sea. Much work also remains to be done to  
941 fully understand the differences in AMOC variability and change between CESM1 and CESM2  
942 and to determine whether we trust one more than the other.

943 Overall, the method-dependence found for the aerosol-forced response in CESM2, raises the  
944 question, what is the more appropriate method to use in single forcing experiments? Our experience  
945 with two generations of CESM indicates that the method used may matter for some models and/or  
946 forcings more than others. Ultimately, there is probably no getting around the non-linearities that  
947 exist in CESM2, particularly that due to the AMOC and one method is not going to necessarily  
948 give you a more correct answer than the other. Using the “only” method we would conclude that  
949 greenhouse gases are giving rise to a dramatic decline in AMOC strength that starts in the mid-20th  
950 century, whereas the reality is that the greenhouse gases don’t have this same effect when they  
951 are imposed together with aerosol forcing. Using the “all-but-one” method we would conclude  
952 that aerosols give rise to an increasing AMOC strength at least out to 2050, but the reality is that  
953 they are only apparently doing that because they have prevented the greenhouse gas-forced AMOC  
954 decline. The AMOC response to forcings is non-linear and neither method alone would provide  
955 the complete picture and we should be aware of such non-linearities in our interpretation.

956 This new CESM2 dataset has been released to the research community and we expect that there  
957 are many more interesting insights that can be gained from it. We also expect that further insights  
958 can be gained by building on the dataset provided here through modified experimental design  
959 and/or forcing combinations. Unlike the CESM1 single forcing large ensemble, this new ensemble

960 offers the opportunity to assess additivity of the different forcing contributions in comparison to the  
961 overall LENS2 response. The results presented here highlight the importance of non-linearities in  
962 interpreting single-forcing simulations, while simultaneously highlighting pertinent mechanisms  
963 underlying these non-linearities that may be of value for future endeavors. It is our hope that future  
964 work will make use of this dataset to further explain the role of individual forcings and identify  
965 their interactions in the evolution of the Earth system.



966 *Acknowledgments.* This work is supported by the National Center for Atmospheric Research,  
967 which is a major facility sponsored by the National Science Foundation under the Cooperative  
968 Agreement 1852977. Computing and data storage resources, including the Cheyenne supercom-  
969 puter (<https://doi.org/10.5065/D6RX99HX>), were provided by the Computational and Information  
970 Systems Laboratory at NCAR. We also acknowledge the Community Earth System Model version  
971 1 Large Ensemble Community Project, the Community Earth System Model version 2 Large En-  
972 semble Community Project and supercomputing resources provided by the IBS Center for Climate  
973 Physics in South Korea (<https://doi.org/10.5194/esd-2021-50>). The CESM2 large ensemble simu-  
974 lations were conducted on the IBS/ICCP supercomputer “Aleph”, a 1.43 petaflop high-performance  
975 Cray XC50-LC Skylake computing system. The work of KBR was supported by the Institute for  
976 Basic Sciences (IBS), Republic of Korea, under IBS-R028-D1. IRS is grateful to Brian Medeiros,  
977 John Fasullo, Robb Jnglin Wills, Andrew Gettelman and Marika Holland for helpful discussions.

978 *Data availability statement.* The CESM1 datasets used in this study are freely avail-  
979 able through NCAR’s Climate Data Gateway with guidance for data access located  
980 at the following website [https://www.cesm.ucar.edu/projects/community-projects/LENS/data-](https://www.cesm.ucar.edu/projects/community-projects/LENS/datasets.html)  
981 [sets.html](https://www.cesm.ucar.edu/projects/community-projects/LENS/datasets.html). The CESM2 large ensemble is also available through NCAR’s Cli-  
982 mate Data Gateway with guidance for data access located at the following website  
983 <https://www.cesm.ucar.edu/projects/community-projects/LENS2/data-sets.html>. The CESM2  
984 single forcing large is available through the Climate Data Gateway as described at  
985 <https://www.cesm.ucar.edu/working-groups/climate/simulations/cesm2-single-forcing-le>. The  
986 analysis codes for reproducing the figures in this manuscript are available at  
987 [https://github.com/islasimpson/singleforcing\\_paper](https://github.com/islasimpson/singleforcing_paper) and the data required to make the figures are  
988 available at <https://doi.org/10.5065/ayy9-fr14>

## 989 APPENDIX

### 990 **Comparison of the anthropogenic aerosol forcing between the CESM2 and CESM1 single** 991 **forcing large ensembles**

992 Given that much of the analysis in this study focusses on the anthropogenic aerosol-forced  
993 response, we provide a comparison of the aerosol forcing between AAER2 and AAER1 in Fig. A1  
994 with a focus on two species (BC and SO<sub>4</sub>), while the emissions and burdens of other species can be

995 found in supplemental Figs. 3 and 4. A comparison of Figs. A1a and A1b reveals that the trends in  
996 anthropogenic aerosol optical depth at 550 nm (AOD) over 2000-2050 are very different between  
997 the AAER2 (historical to SSP3-7.0) and AAER1 (historical to RCP8.5) simulations. AAER1 shows  
998 declines in AOD over eastern North America, Europe and China with relatively small increases  
999 in AOD over Africa and India (Fig. A1b). In AAER2, the declines over eastern North America  
1000 and Europe are much smaller compared to AAER1 and the AOD increases over China in AAER2  
1001 while it decreases in AAER1. Over Africa and India, AOD is increasing much more in AAER2  
1002 than in AAER1. This difference primarily stems from the difference in emissions, but differences  
1003 in the model physics also play a role in the differing overall aerosol burdens between AAER1 and  
1004 AAER2, as now discussed.

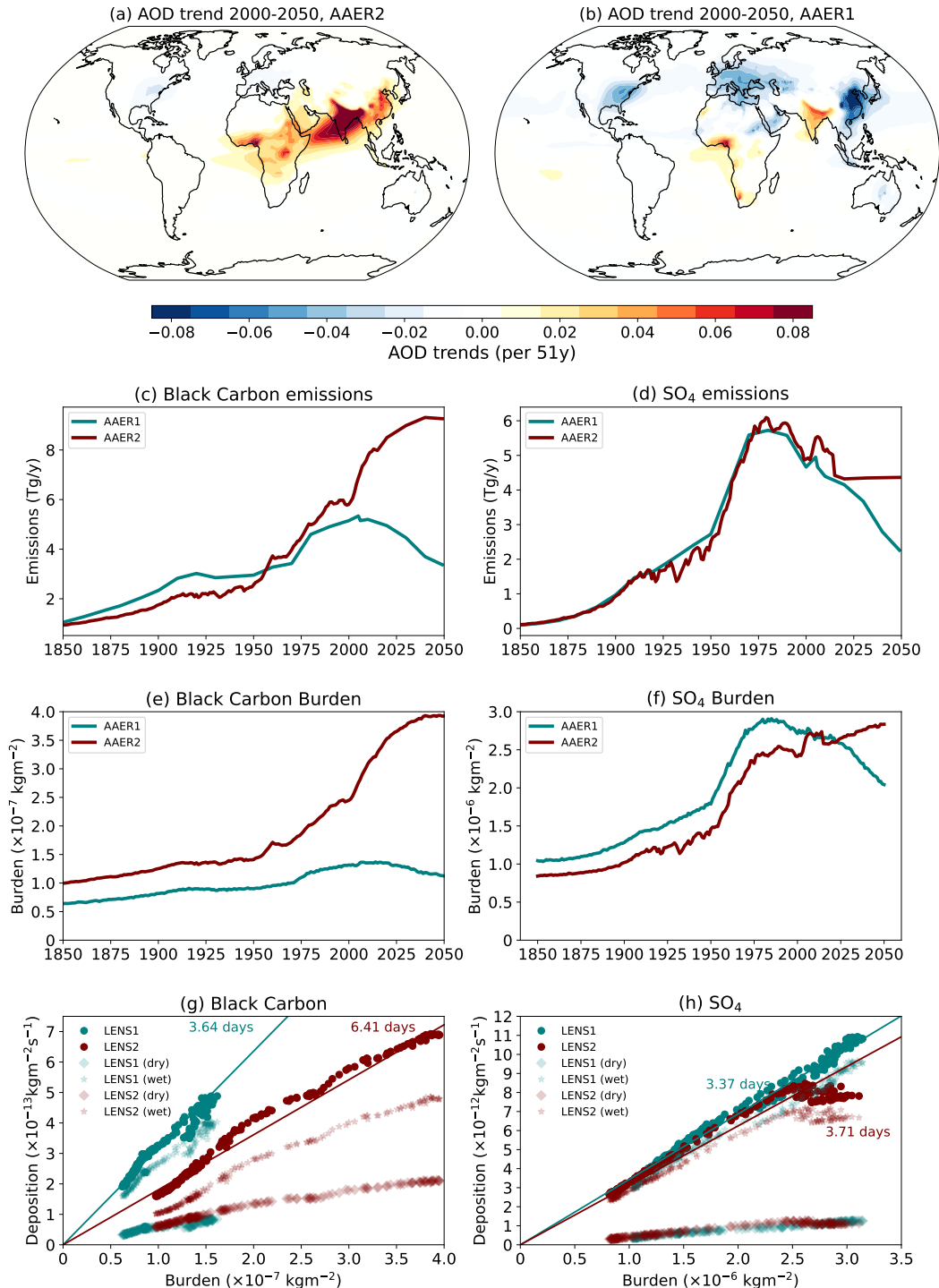
1005 The global BC emissions in AAER1 and AAER2 are fairly similar until about the year 2000,  
1006 but after that they increase in AAER2 and decrease in AAER1 (Fig. A1 c) (a similar trajectory is  
1007 seen for POM in supplemental Fig. 3d). SO<sub>4</sub> emissions are also similar until about the year 2000,  
1008 but then they remain fairly steady in AAER2 while declining in AAER1 (Fig. A1d) (a similar  
1009 trajectory is seen for SO<sub>2</sub> in supplemental Fig. 3c). For BC, while the emissions are slightly lower  
1010 over the 19th and early 20th centuries in AAER2 compared to AAER1 (Fig. A1c), the BC burden  
1011 is higher in AAER2 compared to AAER1 (Fig. A1e). The lifetime of BC, estimated by the ratio  
1012 of the global BC burden to the global BC deposition flux, is longer in CESM2 (6.41 days) than in  
1013 CESM1 (3.64 days, Fig. A1g). This nearly two-fold increase in BC lifetime can be understood as  
1014 resulting from the BC wet deposition flux associated with a given burden being smaller in CESM2  
1015 than in CESM1 and the wet deposition flux has changed because the representation of the aging  
1016 of primary carbonaceous aerosols in CESM2 delays BC removal via wet deposition (section 2.a.1  
1017 and see the differing wet deposition rates at a given global burden in Fig. A1g). For SO<sub>4</sub>, the  
1018 emissions are rather similar over the historical period (Fig. A1d) but the burden (Fig. A1f) is  
1019 higher in AAER1 than in AAER2 for reasons that are not totally clear given that the deposition  
1020 rates are fairly comparable between CESM1 and CESM2 (Fig. A1h).

1021 In summary, the difference in BC and SO<sub>4</sub> emissions is the primary contributor to the difference  
1022 in burden (and associated AOD) trends between AAER2 and AAER1, with some additional  
1023 modification due to the differing model physics. The SSP3-7.0 scenario is a higher aerosol  
1024 emission scenario (Gidden et al. 2019) than the CMIP5 RCP8.5 scenario used in the CESM1 single

1025 forcing large ensemble and the emissions also differ slightly over the historical period as emissions  
1026 inventories were revised between CMIP5 and CMIP6, although it should be noted that it has been  
1027 argued that the increasing emissions over eastern China in the last decade of the historical period in  
1028 the CMIP6 emissions are incorrect (Wang et al. 2021). The impact of such differences in emissions  
1029 can end up being as large as the impact of changing from one model version to the next (e.g., Fyfe  
1030 et al. 2021).

## References

- Allen, R. J., J. R. Norris, and M. Kovilakam, 2014: Influence of anthropogenic aerosols and the Pacific Decadal Oscillation on tropical belt width. *Nature Geoscience*, **7**, 270–274.
- Baek, S. H., Y. Kushnir, M. Ting, J. E. Smerdon, and J. M. Lora, 2022: Regional Signatures of Forced North Atlantic SST Variability: A Limited Role for Aerosols and Greenhouse Gases. *Geophysical Research Letters*, **49**, [https://doi.org/https://doi.org/10.1029/2022GL097794](https://doi.org/10.1029/2022GL097794).
- Bogenschutz, P. A., A. Gettelman, C. Hannay, V. E. Larson, R. B. Neale, C. Craig, and C.-C. Chen, 2018: The path to CAM6: coupled simulations with CAM5.4 and CAM5.5. *Geosci. Model Dev.*, **11**, 235–255.
- Bonfils, C. J. W., B. D. Santer, J. C. Fyfe, K. Marvel, T. J. Phillips, and S. R. H. Zimmerman, 2020: Human influence on joint changes in temperature, rainfall and continental aridity. *Nature Climate Change*, **10**, 726–731.
- Brodeau, L., and T. Koenigk, 2016: Extinction of the northern oceanic deep convection in an ensemble of climate model simulations of the 20th and 21st centuries. *Clim. Dyn.*, **46**, 2863–2882.
- Capotondi, A., C. Deser, A. S. Phillips, Y. Okumura, and S. M. Larson, 2020: ENSO and Pacific decadal variability in the Community Earth System Model version 2. *J. Adv. Mod. Earth Sys.*, **12**, e2019MS002022.
- Chiang, F., O. Mazdiyasi, and A. AghaKouchak, 2021: Evidence of anthropogenic impacts on global drought frequency, duration, and intensity. *Nature Communications*, **12**, 2754, [https://doi.org/https://doi.org/10.1038/s41467-021-22314-w](https://doi.org/10.1038/s41467-021-22314-w).
- Dagan, G., P. Stier, and D. Watson-Parris, 2020: Aerosol Forcing Masks and Delays the Formation of the North Atlantic Warming Hole by Three Decades. *Geophys. Res. Lett.*, **47**, [https://doi.org/https://doi.org/10.1029/2020GL090778](https://doi.org/10.1029/2020GL090778).
- Danabasoglu, G., S. C. Bates, B. P. Briegleb, S. R. Jayne, and W. G. Jochum, M. amd Large, 2012: The CCSM4 ocean component. *J. Clim.*, **25**, 1361–1389.



1031 FIG. A1. (a) and (b) Trends in annual mean AOD at 550nm between 2000 and 2050 of AAER2 and AAER1, respectively. (c)  
 1032 Global annual mean emissions of BC for AAER1 (teal) and AAER2 (maroon). (d) same as (c) but for SO<sub>4</sub> aerosol. (e) Global  
 1033 annual mean BC burden for AAER1 (teal) and AAER2 (maroon). (f) as (e) but for SO<sub>4</sub>. (g) Global annual mean deposition fluxes  
 1034 versus burden for a single member of LENS2 and LENS1 (used rather than the single forcing experiments because the deposition  
 1035 fluxes were not output in the CESM1 single forcing large ensemble). Circles show the full deposition flux (dry + wet), stars show  
 1036 the wet deposition flux and diamonds show the dry deposition flux. (h) as (g) but for SO<sub>4</sub>.

- 1063 Danabasoglu, G., L. Landrum, S. G. Yeager, and P. R. Gent, 2019: Robust and Nonrobust Aspects  
1064 of Atlantic Meridional Overturning Circulation Variability and Mechanisms in the Community  
1065 Earth System Model. *J. Clim.*, **32**, 7349–7368.
- 1066 Danabasoglu, G., and Coauthors, 2020: The Community Earth System Model 2 (CESM2). *J. Adv.*  
1067 *Mod. Earth Sys.*, **12**, <https://doi.org/10.1029/2019MS001916>.
- 1068 Delworth, T. L., and F. Zeng, 2014: Regional rainfall decline in Australia attributed to anthro-  
1069 pogenic greenhouse gases and ozone levels. *Nature Geoscience*, **7**, 583–587.
- 1070 Delworth, T. L., F. Zeng, L. Zhang, R. Zhang, G. Vecchi, and X. Yang, 2017: The Central Role of  
1071 Ocean Dynamics in Connecting the North Atlantic Oscillation to the Extratropical Component  
1072 of the Atlantic Multidecadal Oscillation. *J. Clim.*, **30**, 3789–3805.
- 1073 Deng, J., A. Dai, and H. Xu, 2020: Nonlinear Climate Response to Increasing CO<sub>2</sub> and Anthro-  
1074 pogenic Aerosols Simulated by CESM1. *J. Clim.*, **33**, 281–301.
- 1075 DeRepentigny, P., and Coauthors, 2022: Enhanced simulated early 21st century Arctic sea ice loss  
1076 due to CMIP6 biomass burning emissions. *Science Advances*, **8 (30)**, [https://doi.org/10.1126/](https://doi.org/10.1126/sciadv.abo2405)  
1077 [sciadv.abo2405](https://doi.org/10.1126/sciadv.abo2405).
- 1078 Deser, C., R. A. Tomas, and L. Sun, 2015: The Role of Ocean-Atmosphere Coupling in the Zonal  
1079 Mean Atmospheric Response to Arctic Sea Ice Loss. *J. Clim.*, **28**, 2168–2186.
- 1080 Deser, C., and Coauthors, 2020a: Insights from Earth system model initial-condition large ensem-  
1081 bles and future prospects. *Nat. Clim. Change*, **10**, 277–286.
- 1082 Deser, C., and Coauthors, 2020b: Isolating the Evolving Contributions of Anthropogenic Aerosols  
1083 and Greenhouse Gases: A New CESM1 Large Ensemble Community Resource. *J. Clim.*, **33**,  
1084 7835–7858.
- 1085 Dittus, A. J., E. Hawkins, J. I. Robson, D. M. Smith, and J. Wilcox, L., 2021: Drivers of Recent North  
1086 Pacific Decadal Variability: The Role of Aerosol Forcing. *Earth's Future*, **9**, [https://doi.org/](https://doi.org/https://doi.org/10.1029/2021EF002249)  
1087 <https://doi.org/10.1029/2021EF002249>.

- 1088 Dixon, K. W., T. L. Delworth, M. J. Spelman, and R. J. Stouffer, 1999: The influence of transient  
1089 surface fluxes on North Atlantic overturning in a coupled GCM Climate Change Experiment.  
1090 *Geophys. Res. Lett.*, **26**, 2749–2752.
- 1091 Dong, B., R. T. Sutton, E. Highwood, and L. Wilcox, 2014: The Impacts of European and Asian  
1092 Anthropogenic Sulfur Dioxide Emissions on Sahel Rainfall. *J. Clim.*, **27**, 7000–7017.
- 1093 DuVivier, A. K., M. M. Holland, J. E. Kay, S. Tilmes, A. Gettelman, and D. A. Bailey, 2020:  
1094 Arctic and Antarctic sea ice mean state in the Community Earth System Model version 2 and  
1095 the influence of atmospheric chemistry. *J. Geophys. Res.: Oceans*, **125**, e2019JC015 934.
- 1096 England, M. R., I. Eisenman, N. J. Lutsko, and T. J. W. Wagner, 2021: The Recent Emer-  
1097 gence of Arctic Amplification. *Geophys. Res. Lett.*, **48**, [https://doi.org/https://doi.org/10.1029/  
1098 2021GL094086](https://doi.org/10.1029/2021GL094086).
- 1099 Eyring, V., S. Bony, G. Meehl, C. A. Senior, B. Stevens, R. J. Stouffer, and K. E. Taylor, 2016:  
1100 Overview of the Coupled Model Intercomparison Project Phase 6 (CMIP6) experimental design  
1101 and organization. *Geoscientific Model Development*, **9**, 1937–1958.
- 1102 Fasullo, J. T., P. R. Gent, and R. S. Nerem, 2020: Sea Level Rise in the CESM Large Ensemble:  
1103 The Role of Individual Climate Forcings and Consequences for the Coming Decades. *J. Clim.*,  
1104 **33**, 6911–6927.
- 1105 Fasullo, J. T., J.-F. Lamarque, C. Hannay, N. Rosenbloom, S. Tilmes, P. DeRepentigny, A. Jahn,  
1106 and C. Deser, 2021: Spurious Late Historical-Era Warming in CESM2 Driven by Prescribed  
1107 Biomass Burning Emissions. *Geophys. Res. Lett.*, **49**, e2021GL097 420, <https://doi.org/https://doi.org/10.1029/2021GL097420>.
- 1109 Feichter, J., E. Roeckner, U. Lohmann, and B. Liepert, 2004: Nonlinear Aspects of the Climate  
1110 Response to Greenhouse Gas and Aerosol Forcing. *J. Clim.*, **17**, 2384–2398.
- 1111 Fyfe, J. C., V. V. Kharin, B. D. Santer, J. N. S. Cole, and N. P. Gillett, 2021: Significant impact  
1112 of forcing uncertainty in a large ensemble of climate model simulations. *Proc. Natl. Acad. Sci.  
1113 (USA)*, **118**, e2016549 118.
- 1114 Gettelman, A., and H. Morrison, 2015: Advanced two-moment bulk microphysics for global  
1115 models. Part 2: Off-line tests and comparison with other schemes. *J. Clim.*, **28**, 1268–1287.

- 1116 Gettelman, A., and Coauthors, 2019: The Whole Atmosphere Community Climate Model Version  
1117 6 (WACCM6). *J. Geophys. Res.: Atm*, **124**, <https://doi.org/10.1029/2019JD030943>.
- 1118 Giannini, A., and A. Kaplan, 2019: The role of aerosols and greenhouse gases in Sahel drought  
1119 and recovery. *Climatic Change*, **152**, 449–466.
- 1120 Gidden, M. J., and Coauthors, 2019: Global emissions pathways under different socioeconomic  
1121 scenarios for use in CMIP6: a dataset of harmonized emissions trajectories through the end of  
1122 the century. *Geosci. Model Dev.*, **12**, 1443–1475.
- 1123 Gillett, N. P., and Coauthors, 2016: The Detection and Attribution Model Intercomparison Project  
1124 (DAMIP v1.0) contribution to CMIP6. *Geosci. Model Dev.*, **9**, 3685–3697.
- 1125 Gillett, N. P., and Coauthors, 2021: Constraining human contributions to observed warming since  
1126 the pre-industrial period. *Nat. Clim. Change*, **11**, 207–212.
- 1127 Hassan, T., R. J. Allen, W. Liu, and C. A. Randles, 2021: Anthropogenic aerosol forcing of the  
1128 Atlantic meridional overturning circulation and the associated mechanisms in CMIP6 models.  
1129 *Atmos. Chem. Phys.*, **21**, 5821–5846.
- 1130 Hassan, T., and Coauthors, 2022: Air quality improvements are projected to weaken the Atlantic  
1131 meridional overturning circulation through radiative forcing effects. *Nature Communications  
1132 Earth and Environment*, **3**, <https://doi.org/10.1038/s43247-022-00476-9>.
- 1133 Hirasawa, H., P. J. Kushner, M. Sigmond, J. Fyfe, and C. Deser, 2020: Anthropogenic Aerosols  
1134 Dominate Forced Multidecadal Sahel Precipitation Change through Distinct Atmospheric and  
1135 Oceanic Drivers. *J. Clim.*, **33**, 10 187–10 204.
- 1136 Hunke, E. C., W. H. Lipscomb, A. K. Turner, N. Jeffery, and S. Elliott, 2015: Cice: The los alamos  
1137 sea ice model. documentation and software user’s manual. version 5.1. Tech. Rep. LA-CC-06-  
1138 012, iT-3 Fluid Dynamics Group, Los Alamos National Laboratory.
- 1139 Hurrell, J. W., and Coauthors, 2013: The Community Earth System Model: A Framework for  
1140 Collaborative Research. *Bull. Amer. Meteor. Soc.*, **94**, 1339–1360.
- 1141 IPCC, 2021: Summary for Policy Makers. In: Climate Change 2021: The Physical Science Basis.  
1142 Contribution of Working Group 1 to the Sixth Assessment Report of the Intergovernmental



- 1143 Panel on Climate Change. Tech. rep., Cambridge University Press, Cambridge, United Kingdom  
1144 and New York, NY, USA, 3-32 pp. <https://doi.org/10.1017/9781009157896.001>.
- 1145 Jahn, A., and M. M. Holland, 2013: Implications of Arctic sea ice changes for North Atlantic deep  
1146 convection and the meridional overturning circulation in CCSM4-CMIP5 simulations. *Geophys.*  
1147 *Res. Lett.*, **40**, 1206–1211.
- 1148 Kay, J. E., and Coauthors, 2015: The Community Earth System Model (CESM) Large Ensemble  
1149 Project. *Bull. Amer. Meteor. Soc.*, **96**, 1333–1349.
- 1150 Lamarque, J. F., G. P. Kyle, M. Meinshausen, K. Riahi, S. J. Smith, D. P. van Vuuren, A. J. Conley,  
1151 and F. Vitt, 2011: Global and regional evolution of short-lived radiatively active gases and  
1152 aerosols in the Representative Concentration Pathways. *Climatic Change*, **109**, 191–212.
- 1153 Large, W. G., G. Danabasoglu, S. C. Doney, and J. C. McWilliams, 1997: Sensitivity to surface  
1154 forcing and boundary layer mixing in the NCAR CSM ocean model: Annual-mean climatology.  
1155 *J. Phys. Oceanogr.*, **27**, 2418–2447.
- 1156 Lawrence, D., and Coauthors, 2019: The Community Land Model, version 5: Description of  
1157 new features, benchmarking and impact of forcing uncertainty. *J. Adv. Mod. Earth Sys.*, **11**,  
1158 4245–4287.
- 1159 Lawrence, D. M., and Coauthors, 2011: Parameterization improvements and functional and  
1160 structural advances in Version 4 of the Community Land Model. *J. Adv. Mod. Earth Sys.*,  
1161 **3**, <https://doi.org/https://doi.org/10.1029/2011MS00045>.
- 1162 Li, H., A. Federov, and W. Liu, 2021: AMOC Stability and Diverging Response to Arctic Sea Ice  
1163 Decline in Two Climate Models. *J. Clim.*, **34**, 5443–5460.
- 1164 Li, X., M. Ting, and D. E. Lee, 2018: Fast Adjustments of the Asian Summer Monsoon to  
1165 Anthropogenic Aerosols. *Geophys. Res. Lett.*, **45**, 1001–1010, [https://doi.org/https://doi.org/10.](https://doi.org/https://doi.org/10.1002/2017GL076667)  
1166 [1002/2017GL076667](https://doi.org/https://doi.org/10.1002/2017GL076667).
- 1167 Liu, X., P.-L. Ma, H. Wang, S. Tilmes, B. Singh, R. C. Easter, S. J. Ghan, and P. J. Rasch, 2016:  
1168 Description and evaluation of a new four-mode version of the Model Aerosol Module (MAM4)  
1169 within version 5.3 of the Community Atmosphere Model. *Geosci. Model Dev.*, **9**, 505–522.

- 1170 Liu, X., and Coauthors, 2012: Toward a minimal representation of aerosols in climate models:  
1171 description and evaluation in the Community Atmosphere Model CAM5. *Geosci. Model Dev.*,  
1172 **5**, 709–739.
- 1173 Lombardozzi, D. L., Y. Lu, P. J. Lawrence, D. M. Lawrence, S. Swenson, K. W. Oleson, W. R.  
1174 Wieder, and E. A. Ainsworth, 2020: Simulating agriculture in the community land model version  
1175 **5**. *J. Geophys. Res.: Biogeosciences*, **125**, e2019JG005 529.
- 1176 Manabe, S., and R. J. Stouffer, 1993: Century-scale effects of increased atmospheric CO<sub>2</sub> on the  
1177 ocean-atmosphere system. *Nature*, **364**, 215–217.
- 1178 McDougall, T. J., D. R. Jackett, D. G. Wright, and R. Feistel, 2003: Accurate and Computationally  
1179 Efficient Algorithms for Potential Temperature and Density of Seawater. *Journal of Atmospheric  
1180 and Oceanic Technology*, **20**, 730–741.
- 1181 Meehl, G. A., C. Shields, J. M. Arblaster, H. Annamalai, and R. Neale, 2020: Intraseasonal,  
1182 Seasonal, and Interannual Characteristics of Regional Monsoon Simulations in CESM2. *J. Adv.  
1183 Mod. Earth Sys.*, **12**, [https://doi.org/https://doi.org/10.1029/2019MS001962](https://doi.org/10.1029/2019MS001962).
- 1184 Meehl, G. A., W. M. Washington, C. M. Ammann, J. M. Arblaster, T. M. L. Wigley, and C. Tebaldi,  
1185 2004: Combinations of Natural and Anthropogenic Forcings in Twentieth-Century Climate. *J.  
1186 Clim.*, **17**, 3721–3727.
- 1187 Meinshausen, M., and Coauthors, 2011: The RCP greenhouse gas concentrations and their exten-  
1188 sions from 1765 to 2300. *Climatic Change*, **109**, 213–241.
- 1189 Meinshausen, M., and Coauthors, 2020: The shared socio-economic pathway (SSP) greenhouse  
1190 gas concentrations and their extensions to 2500. *Geosci. Model Dev.*, **13**, 3571–3605.
- 1191 Menary, M. B., J. Robson, R. P. Allan, B. B. B. Booth, C. Cassou, and G. Gastineau, 2020:  
1192 Aerosol-forced AMOC changes in CMIP6 historical simulations. *Geophys. Res. Lett.*, **47**,  
1193 e2020GL088 166.
- 1194 Ming, Y., and V. Ramaswamy, 2009: Nonlinear Climate and Hydrological Responses to Aerosol  
1195 Effects. *J. Clim.*, **22**, 1329–1339.

- 1196 Monerie, P.-A., L. J. Wilcox, and A. G. Turner, 2022: Effects of Anthropogenic Aerosol and  
1197 Greenhouse Gas Emissions on Northern Hemisphere Monsoon Precipitation: Mechanisms and  
1198 Uncertainty. *J. Clim.*, **35**, 2305–2326.
- 1199 Morrison, H., and A. Gettelman, 2008: A new two-moment bulk stratiform cloud microphysics  
1200 scheme in the NCAR Community Atmosphere Model (CAM3). Part 1: Description and numer-  
1201 ical tests. *J. Clim.*, **21**, 3642–3659.
- 1202 Mueller, B. L., N. P. Gillett, A. H. Monahan, and F. W. Zwiers, 2018: Attribution of Arctic Sea  
1203 Ice Decline from 1953 to 2012 to Influences from Natural, Greenhouse Gas and Anthropogenic  
1204 Aerosol Forcing. *J. Clim.*, **31**, 7771–7787.
- 1205 Pendergrass, A. G., D. B. Coleman, C. Deser, F. Lehner, N. Rosenbloom, and I. R. Simpson, 2019:  
1206 Nonlinear Response of Extreme Precipitation to Warming in CESM1. *Geophys. Res. Lett.*, **46**,  
1207 10 551–10 560.
- 1208 Robson, J., and Coauthors, 2022: The role of anthropogenic aerosol forcing in the 1850-1985  
1209 strengthening of the AMOC in CMIP6 historical simulations. *J. Clim.*, <https://doi.org/https://doi.org/10.1175/JCLI-D-22-0124.1>.
- 1211 Rodgers, K. B., and Coauthors, 2021: Ubiquity of human-induced changes in climate variability.  
1212 *Earth Sys. Dynam.*, **12**, 1393–1411.
- 1213 Seong, M., S. Min, Y. Kim, X. Zhang, and Y. Sun, 2021: Anthropogenic Greenhouse Gas and  
1214 Aerosol Contributions to Extreme Temperature Changes during 1951-2015. *J. Clim.*, **34**, 857–  
1215 870.
- 1216 Shi, J.-R., Y.-O. Kwon, and S. Wijffels, 2022: Two Distinct Modes of Climate Responses to the  
1217 Anthropogenic Aerosol Forcing Changes. *J. Clim.*, **35**, 3445–3457.
- 1218 Simpson, I. R., D. M. Lawrence, S. C. Swenson, C. Hannay, K. A. McKinnon, and J. E. Truesdale,  
1219 2022: Improvements in Wintertime Surface Temperature Variability in the Community Earth  
1220 System Model Version 2 (CESM2) Related to the Representation of Snow Density. *J. Adv. Mod.*  
1221 *Earth Sys.*, **14**, e2021MS002 880.

- 1222 Simpson, I. R., and Coauthors, 2020: An evaluation of the large-scale atmospheric circulation  
1223 and its variability in CESM2 and other CMIP models. *J. Geophys. Res.: Atmospheres*, **125**,  
1224 e2020JD032835.
- 1225 Singh, D., S. P. McDerimid, B. I. Cok, M. J. Puma, L. Nazarenko, and M. Kelley, 2018: Distinct  
1226 Influences of Land Cover and Land Management on Seasonal Climate. *J. Geophys. Res. Atm.*,  
1227 **123**, 12017–12039, <https://doi.org/https://doi.org/10.1029/2018JD028874>.
- 1228 Smith, D., and Coauthors, 2022: Attribution of multi-annual to decadal changes in the climate sys-  
1229 tem: The Large Ensemble Single Forcing Model Intercomparison Project (LESFMIP). *Frontiers*  
1230 *in Climate*, <https://doi.org/10.3389/fclim.2022.955414>.
- 1231 Smith, R., and Coauthors, 2010: The Parallel Ocean Program (POP) reference manual, Ocean  
1232 component of the Community Climate System Model (CCSM). Tech. rep., LANL Tech. Report.,  
1233 141 pp. <https://doi.org/LAUR%2010%201853>.
- 1234 Tilmes, S., and Coauthors, 2019: Climate Forcing and Trends of Organic Aerosols in the Commu-  
1235 nity Earth System Model (CESM2). *J. Adv. Mod. Earth Sys.*, **11**, 4323–4351.
- 1236 Touma, D., S. Stevenson, F. Lehner, and S. Coats, 2021: Human-driven greenhouse gas and aerosol  
1237 emissions cause distinct regional impacts on extreme fire weather. *Nature Communications*, **12**,  
1238 <https://doi.org/https://doi.org/10.1038/s41467-020-20570-w>.
- 1239 Undorf, S., D. Polson, M. A. Bollasina, Y. Ming, A. Schurer, and G. C. Hegerl, 2018: Detectable  
1240 Impact of Local and Remote Anthropogenic Aerosols on the 20th Century Changes of West  
1241 African and South Asian Monsoon Precipitation. *J. Geophys. Res. Atm.*, **123**, 4871–4889.
- 1242 van Marle, M. J. E., and Coauthors, 2017: Historic global biomass burning emissions based on  
1243 merging satellite observations with proxies and fire models (1750-2015). *Geosci. Model Dev.*  
1244 *Discuss.*, **10**, 3329–3357, <https://doi.org/https://doi.org/10.5194/gmd-10-3329-2017>.
- 1245 Wang, K., C. Deser, L. Sun, and R. A. Tomas, 2018: Fast Response of the Tropics to an Abrupt  
1246 Loss of Arctic Sea Ice via Ocean Dynamics. *Geophys. Res. Lett.*, **45**, <https://doi.org/https://doi.org/10.1029/2018GL077325>.
- 1248 Wang, Z., and Coauthors, 2021: Incorrect Asian aerosols affecting the attribution and projection  
1249 of regional climate change in CMIP6 models. *npj Clim Atmos Sci*, **4**.

- 1250 Watanabe, M., and H. Tatebe, 2019: Reconciling roles of sulphate aerosol forcing and internal  
1251 variability in Atlantic multidecadal climate changes. *Climate Dynamics*, **53**, 4651–4665.
- 1252 Weaver, A. J., M. Eby, M. Kienast, and O. A. Saenko, 2007: Response of the Atlantic merid-  
1253 ional overturning circulation to increasing atmospheric CO<sub>2</sub>: sensitivity fo mean climate state.  
1254 *Geophys. Res. Lett.*, **34**, L05708.
- 1255 Wieder, W. R., D. Kennedy, F. Lehner, K. N. Musselman, K. B. Rodgers, N. Rosenbloom, I. R.  
1256 Simpson, and R. Yamaguchi, 2022: Pervasive alterations to snow-dominated ecosystem func-  
1257 tions under climate change. *Proc. Nat. Ac. Sci*, **119**, [https://doi.org/https://doi.org/10.1073/pnas.](https://doi.org/https://doi.org/10.1073/pnas.2202393119)  
1258 [2202393119](https://doi.org/https://doi.org/10.1073/pnas.2202393119).
- 1259 Yang, Q., T. H. Dixon, P. G. Myers, J. Bonin, D. Chambers, M. R. van den Broeke, M. H.  
1260 Ribergaart, and J. Mortensen, 2016: Recent increases in Arctic freshwater flux affects Labrador  
1261 Sea convection and Atlantic overturning circulation. *Nature Communications*, **7**, 10 525.
- 1262 Zhang, S., P. Stier, G. Dagan, and M. Wang, 2021: Anthropogenic Aerosols Modulated 20th-  
1263 Century Sahel Rainfall Variability Via Their Impacts on North Atlantic Sea Surface Temperature.  
1264 *Geophys. Res. Lett.*, **49**, <https://doi.org/https://doi.org/10.1029/2021GL095629>.